Materials Science & Engineering A 885 (2023) 145617

Contents lists available at ScienceDirect

Materials Science & Engineering A

journal homepage: www.elsevier.com/locate/msea

Blown-powder direct-energy-deposition of titanium-diboride-strengthened IN718 Ni-base superalloy

Riddhi Sarkar [a,c,*], Bo Chen [b], Michael E. Fitzpatrick [c], Tim Hilditch [d], Daniel Fabijanic [a]

[a] Institute for Frontier Materials, Deakin University, Waurn Ponds, Victoria, 3216, Australia
[b] School of Engineering, University of Leicester, Leicester, LE1 7RH, UK
[c] The Institute for Future Transport and Cities, Coventry University, Coventry, CV1 5FB, UK
[d] School of Engineering, Deakin University Waurn Ponds, Victoria, 3216, Australia

ARTICLE INFO

Keywords:
Direct energy deposition
Inconel 718
Microstructure
Inoculant
Tensile properties

ABSTRACT

This paper reports on the adoption of TiB_2 as an inoculant to fabricate IN718 via the direct energy deposition (DED) process. Effective grain refinement and low texture were achieved in IN718/TiB_2 using a TiB_2 powder size of d_{90} = 10 μm and mass fraction of 1.5 wt%. The use of low linear energy density (33.08 J/mm) produced IN718/TiB_2 deposits free from large grains (>300 μm), however at the cost of the formation of interlayer defects. By comparison, the large grains were present in deposits made with a linear energy density of 78.74 J/mm and also in deposits manufactured without an included inoculant. Production of deposits at lower energies without interlayer defects was possible by reducing the powder flow rate to 7 g/min. However, this caused a moderate increase in grain size. The TiB_2 inoculant reduced the Laves phase network by replacing it with homogeneously distributed Cr-, Mo-, Nb-, and B-enriched needle-shaped precipitates. Tensile strength increased by 300–500 MPa with TiB_2 addition, but at the cost of significant ductility drop, regardless of the deposition conditions. The IN718 deposit displayed many micro-cracks at the network of Laves phase during tensile loading, whereas micro-cracks in the IN718/TiB_2 occurred at the interface between the needle-shaped precipitates and the matrix. The strength enhancement in IN718/TiB_2 was by a combination of strengthening mechanisms: grain boundary, dislocation structure formation, Orowan-type and load transfer related to the needle-shaped precipitates.

1. Introduction

The microstructure and mechanical properties of Inconel 718 (IN718) fabricated using various additive manufacturing (AM) techniques have been extensively studied [1–5]. Direct energy deposition (DED) is a blown-powder AM process, and during the deposition heat flow occurs towards the substrate through the previously deposited layers, resulting in columnar dendrites growing epitaxially from the substrate. Elongated grains with a {001} texture often result in anisotropic mechanical properties of the AM-fabricated IN718 [2,6–9]. Moreover, high cooling rates associated with the DED inhibits formation of γ″ and γ′ precipitates, and the non-equilibrium solidification promotes the formation of the Nb-enriched Laves phase of $(Ni,Cr,Fe)_2(Nb,Mo,Ti)$ [10,11]. Despite the enhanced strength after post-processing heat treatment due to the precipitation of γ′ and γ′′, anisotropy still exists, especially in the ductility [12–14].

Different solidification modes (columnar or equiaxed) are generally attributed to the thermal gradient G (K/m) and solidification rate R (m/s), which are controlled by process parameters such as laser beam power and travel speed [15,16]. Gäumann et al. [17] developed process maps to predict the columnar-to-equiaxed transformation where a lower G/R ratio favours equiaxed microstructure. Additionally, $G \times R$ represents the cooling rate, and a higher value would result in a finer microstructure, and vice versa. Process parameters can be adjusted to achieve different grain morphologies varying from fully columnar grains to mixed equiaxed and columnar grains in AM-fabricated IN718 [18,19]. However, the inherent high thermal gradient of laser AM restricts the formation of a homogenous equiaxed microstructure [20]. Babu et al. [21] applied theoretical models to electron beam melting (EBM) of IN718 to understand the effect of pre-existing nuclei on the G/R map and observed that higher pre-existing nuclei aids formation of equiaxed grains.

Inoculant particles have been used to modify the microstructure by promoting columnar to equiaxed transition in AM-fabricated aluminium

* Corresponding author. Institute for Frontier Materials, Deakin University, Waurn Ponds, Victoria, 3216, Australia.
E-mail addresses: rsarkar@deakin.edu.au, riddhi.mme@gmail.com (R. Sarkar).

https://doi.org/10.1016/j.msea.2023.145617
Received 23 April 2023; Received in revised form 23 August 2023; Accepted 25 August 2023
Available online 26 August 2023
0921-5093/© 2023 The Authors. Published by Elsevier B.V. This is an open access article under the CC BY-NC-ND license (http://creativecommons.org/licenses/by-nc-nd/4.0/).

alloys [22–24], stainless steels [25–29], titanium alloys [30,31] and high-entropy alloys [32]. The addition of inoculant particles provided strengthening in the resulting deposits, with almost all revealing improved tensile strength at the cost of ductility [27,32,33]. For a wide range of alloy systems, the inoculant has been found to decompose to produce heterogeneous nucleation sites for grain refinement and strengthening of the resulting composite, such as boron nitride nano-tube strengthened Ti–6Al–4V fabricated by DED [33], VC_x strengthened 316L stainless steel fabricated using Laser Powder Bed Fusion (L-PBF) [27], as well as WC_{1-x} [34] and SiC [35] reinforced IN718 fabricated by L-PBF.

Generally, high melting point particles are incorporated as the inoculant to tailor mechanical properties in AM IN718 composites. Ho et al. [36] observed the presence of fine grains in L-PBF IN718 after WC-W_2C addition (0.5 wt%). However, the presence of fine grains was observed only in the matrix adjacent the inoculant surface. TiC was used by Jia et al. [37] and Gu et al. [38] to improve strength and wear performance in L-PBF IN718. The IN718/TiC composites exhibited improved wear properties as compared to IN718 deposits, with high nano-hardness of 4.48 GPa, low friction coefficient of 0.36, and low wear rate of 3.83×10^{-4} mm^3/Nm. However, there was no report about the effect of TiC addition on the microstructure morphology. Ho et al. [39] observed that the addition of $CoAl_2O_4$ particles (0.2 wt%) in L-PBF IN718 resulted in the dispersion of Al-rich nano-oxide particles in the matrix. Overall, they observed creep life increase from 177 to 229 h as a result of inoculant addition. The degree of crystallographic texture and property anisotropy were reduced, but with limited grain refinement. Kong et al. [40] added 10 vol percent of Ti_2AlC to DED IN718 with the objective of modifying the solidification pathway and subsequently observed reduced Laves phase and ~70% increase in yield strength (and ~50% reduction in ductility) due to the formation of (Nb,Ti)(C,N) particles and γ' nanoprecipitate phase. Addition of a large volume fraction of WC during DED processing of IN718 in order to form a MMC was found to strengthen and improve wear resistance of the resulting deposits with the friction coefficient reducing from 0.5 with WC addition compared to 0.6 without WC [41].

The above-mentioned literature survey suggests far less work performed on the DED IN718 with the addition of particles for inoculation or property modification, in comparison to L-PBF. The present work explores the effect of TiB_2 on the microstructure of DED IN718. The effect of the addition of TiB_2 on the mechanical properties of IN718/TiB_2 is determined using tensile tests with the loading applied both parallel and perpendicular to the build direction.

2. Material and experimental procedure

2.1. Selection of inoculant

The selection of TiB_2 as an inoculant is a critical part of the current investigation that deserves some elaboration. In cast IN718 CrFeNb and Co_3FeNb_2 have been identified as efficient inoculants for grain refinement [13,42,43] based on the crystallographic model. The model indicates that both have three distinct matching crystal planes and thus a very low degree of disregistry with the Ni matrix lattice. However, the low melting point of ~1650 °C for these compounds makes them unsuitable for laser DED, where high melt pool temperatures of ~2500 °C are expected [44].

The edge-to-edge matching model proposed by Zhang et al. [45] was used in the present study to calculate the lattice mismatch with the aim of identifying a compatible inoculant for the IN718 manufactured by laser DED. The edge-to-edge model is governed by minimisation of the strain energy of the interface (fully or partially coherent) and considers both the morphology and the orientation relationship (OR) between the matrix and inoculant. Pure FCC structured Ni has a lattice parameter of $a = 0.3524$ nm, however the presence of additional alloying elements (Fe, Cr, Mo) in the IN718 FCC matrix phase results in a larger value of $a = 0.3586$ nm [13]. The close-packed and nearly close-packed directions in IN718 (Ni) are ⟨110⟩, ⟨100⟩ and ⟨112⟩. For the close-packed and nearly close-packed planes of {111}, {200} and {220} in IN718 (Ni), the {111} plane contains the directions of ⟨110⟩ and ⟨112⟩; {200} plane contains ⟨100⟩ and ⟨112⟩ directions, and {220} plane contains all the directions. TiB_2 has a hexagonal crystal structure, with three Ti and six B atoms per unit cell. TiB_2 has four close-packed and nearly close-packed directions of ⟨0001⟩, $\langle \bar{1}\bar{1}23 \rangle$, $\langle 10\bar{1}0 \rangle$ and $\langle 11\bar{2}0 \rangle$, as well as four close-packed and nearly close-packed planes of $\{10\bar{1}1\}$, $\{10\bar{1}\,0\}$, {0001} and $\{11\bar{2}\,0\}$ [45]. From the JCPDS database, the TiB_2 lattice parameters are identified as $a = 0.303$ nm and $c = 0.323$ nm.

The combination of close-packed planes and directions can form 12 direction pairs and 12 plane pairs between TiB_2 and IN718 (Ni) matrix. Table 1 summarises the calculated mismatch of these plane pairs and direction pairs, using the edge-to-edge model. It can be concluded that three possible direction pairs with the mismatch of <10% are: $\langle 110 \rangle_{Ni} / \langle 10\bar{1}0 \rangle_{TiB_2}$, $\langle 100 \rangle_{Ni} / \langle 0001 \rangle_{TiB_2}$, and $\langle 112 \rangle_{Ni} / \langle \bar{1}\bar{1}23 \rangle_{TiB_2}$. Similarly, the matching plane pairs (with mismatch of <10%) are: $\{111\}_{Ni} / \{10\bar{1}1\}_{TiB_2}$, $\{200\}_{Ni} / \{0001\}_{TiB_2}$ and $\{220\}_{Ni} / \{10\bar{1}0\}_{TiB_2}$. The possible ORs between the TiB_2 and IN718 (Ni) matrix are thus identified as follows:

$$(111)_{Ni} \,/\, (10\bar{1}1)_{TiB_2} \parallel [11\bar{2}]_{Ni} \,/\, [\bar{1}\bar{1}23]_{TiB_2}$$

$$(200)_{Ni} \,/\, (0001)_{TiB_2} \parallel [011]_{Ni} \,/\, [\bar{1}010]_{TiB_2}$$

$$(220)_{Ni} \,/\, (10\bar{1}0)_{TiB_2} \parallel [1\bar{1}2]_{Ni} \,/\, [\bar{1}2\bar{1}3]_{TiB_2}$$

$$(220)_{Ni} \,/\, (10\bar{1}0)_{TiB_2} \parallel [001]_{Ni} \,/\, [0001]_{TiB_2}$$

In addition to exhibiting low crystallographic mismatch, TiB_2 has a melting temperature of $T_m > 3000$ °C, which can potentially survive during the DED process. This helps facilitating heterogeneous nucleation sites to disrupt the columnar microstructure. To summarise, considering the high melting temperature and good crystallographic match, TiB_2 is judged as the suitable inoculant for the present study.

2.2. Material preparation and additive manufacturing

Inconel 718 powders used for the DED processed deposits had a size range from 45 μm to 140 μm and were acquired from AP&C pvt. Limited

Table 1
Atomic mismatch between IN718 and TiB_2.

Direction Ni	Direction TiB_2	% Mismatch	Plane Ni	Plane TiB_2	% Mismatch
Ni < 110>	$< 11\bar{2}0 >$	−19.80	Ni {111}	$\{10\bar{1}1\}$	1.36
	< 0001 >	−27.74		$\{10\bar{1}\,0\}$	−27.07
	[a]$< \bar{1}\bar{1}23 >$	12.43		[b]{0001}	21.77
	[a]$< 10\bar{1}0 >$	−3.76		$\{11\bar{2}\,0\}$	26.63
Ni < 100>	$< 11\bar{2}0 >$	15.28	Ni {200}	$\{10\bar{1}1\}$	−13.89
	< 0001 >	9.67		$\{10\bar{1}\,0\}$	−46.73
	$< \bar{1}\bar{1}23 >$	−23.84		{0001}	9.67
	$< 10\bar{1}0 >$	−46.73		$\{11\bar{2}\,0\}$	15.28
Ni < 112>	$< 11\bar{2}0 >$	30.82	Ni {220}	[b]$\{10\bar{1}1\}$	19.46
	< 0001 >	26.24		$\{10\bar{1}\,0\}$	−3.76
	$< \bar{1}\bar{1}23 >$	−1.11		[b]{0001}	−27.74
	$< 10\bar{1}0 >$	−19.80		$\{11\bar{2}\,0\}$	−19.80

[a] Two interatomic spacings in TiB_2 match one spacing in IN718.
[b] Two interplanar spacings in IN718 match one interplanar spacing in TiB_2.

(GE additive). Chemical composition of the feedstock IN718 powders is provided in Table 2. The IN718 powders were spherical without any significant surface or morphological defects, as shown in Fig. 1a. A Camsizer analyser equipped with an optical system was used for determining the powder size distribution. The cumulative distribution (Fig. 1b) reveals values of $d_{50} = 80$ μm and $d_{90} = 105$ μm. TiB_2 particles with three sizes smaller than the IN718 powders, $d_{90} = 1$ μm, $d_{90} = 10$ μm and $d_{90} = 40$ μm, and at three load fractions of 0.5 wt%, 1.5 wt% and 2.5 wt%, were considered. TiB_2 powders were premixed with the feedstock IN718 powders using ball milling, and this process was performed in an argon atmosphere with a powder-to-ball ratio of 1:1, a rotational speed of 200 RPM and for a duration of 6 h. The milled powders were dried in a vacuum furnace at 120 °C for 1.5 h. This process was designed to create a uniform distribution of the inoculant TiB_2 powders on the feedstock IN718 powders, while being mechanically gentle as not to compromise the sphericity of the IN718 powder.

An Optomec LENS MR-7 apparatus equipped with a 1 kW IPG fibre laser with a coaxial powder delivery system was used for the DED processing. The process window was determined by performing several depositions with varying laser power between 350 W and 825 W and scan speed between 6.35 mm/s and 14.8 mm/s. The combined effect of laser power (P) and the scan speed (v) was investigated using linear energy density (E_l) as calculated using the equation $E_l = P/v$ [19]. A higher E_l results in a larger melt pool with higher temperature [2]. Depending on the densification and grain morphologies, two E_l values were adopted to produce High Energy (HE) and Low Energy (LE) deposits. The process parameters are summarised in Table 3; henceforth High Energy ($E_l = 78.74$ J/mm) and Low Energy ($E_l = 33.08$ J/mm) are used throughout the paper. The laser spot size of 1.2 mm was used for all the depositions, and the oxygen content inside the building chamber was kept below 3 ppm during the deposition. An alternating scanning pattern was used, as schematically shown in Fig. 2 (a). An initial powder flow rate of 12 g/min was applied, however lower values were also explored, for reasons explained in the relevant section of the paper. The IN718 substrate plate was solution treated at 980 °C and double aged at 720 °C for 8 h followed by 620 °C for 8 h. The average hardness of the substrate plate was measured as Hv 410 ± 20.

2.3. Microstructural characterisation

Scanning electron microscopy (SEM) and X-ray diffraction (XRD) were performed on the z-x plane of the deposited sample, Fig. 2b. To prepare samples for microstructural characterisation, the deposits were machined from the substrate and sectioned. The sectioned samples were ground using 240-grit to 1200-grit emery papers, and subsequently polished using liquid diamond suspensions down to 1 μm and finally with colloidal silica suspension. A Zeiss SUPRA 55-VP FEGSEM equipped with an electron backscatter diffraction (EBSD) detector from Oxford Instruments was used to measure the grain size and texture. A step size of 2.5 μm was used to collect the EBSD data, unless otherwise stated. The grain size measurements were performed using the circle equivalent diameter generated by the HKL Channel 5 software. Moreover, for the convenience of comparison, the maximum multiple of uniform density (MUD) value for the pole figures was set to 8.0. XRD scans were conducted using an X'Pert Pro MRD XL X-ray diffractometer over a 2θ range of 20° to 100°.

2.4. Mechanical testing

Hardness measurements were performed with a Struers

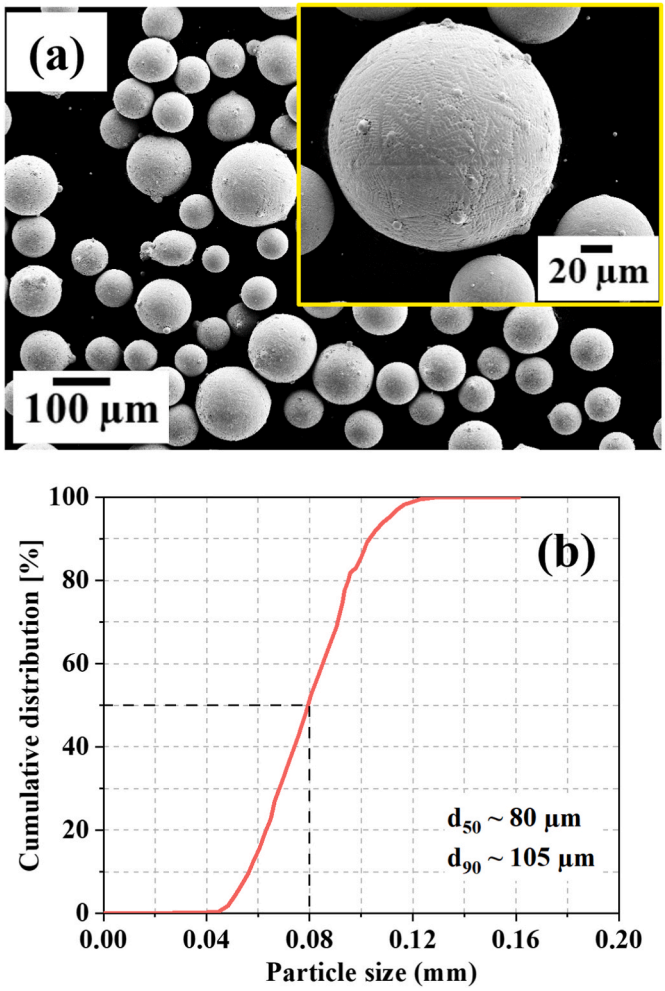

Fig. 1. (a) SEM images of IN718 powders and (b) their size distribution.

Table 3
DED deposition parameters.

Power (W)	Scan Speed (mm/s)	Hatch Spacing (mm)	Layer Thickness (mm)	Flow Rate (g/min)	Linear Energy Density (J/mm)
500	6.3	0.95	0.48	12	78.74 High Energy (HE)
350	10.6	0.60	0.28	12	33.08 Low Energy (LE)

Microhardness tester equipped with a Vickers indenter by applying a 500 gf load and dwell time of 15 s. The reported hardness value represents the average of ~10 indents per condition. IN718 and IN718/TiB_2 samples with dimensions of 12 × 12 × 50 mm^3 were machined from the deposition plate. Sections were taken both vertical and horizontal to the build direction and were sized to tensile test samples (12.5 mm in gauge length and 3 mm in width) using wire-EDM as per the ASTM E8 standard (Fig. 2c). Uniaxial tensile tests were conducted at room temperature under a nominal strain rate of 1×10^{-3} s^{-1} using a ±100 kN Instron servohydraulic universal testing unit equipped with Bluehill 3 software.

Table 2
Chemical composition of feedstock IN718 powders.

Element	Ni	Cr	Nb	Mo	Al	Ti	Mn	Si	C	Fe
Wt %	53.19	18.2	5.04	3.07	0.54	0.96	0.04	0.06	0.05	Bal

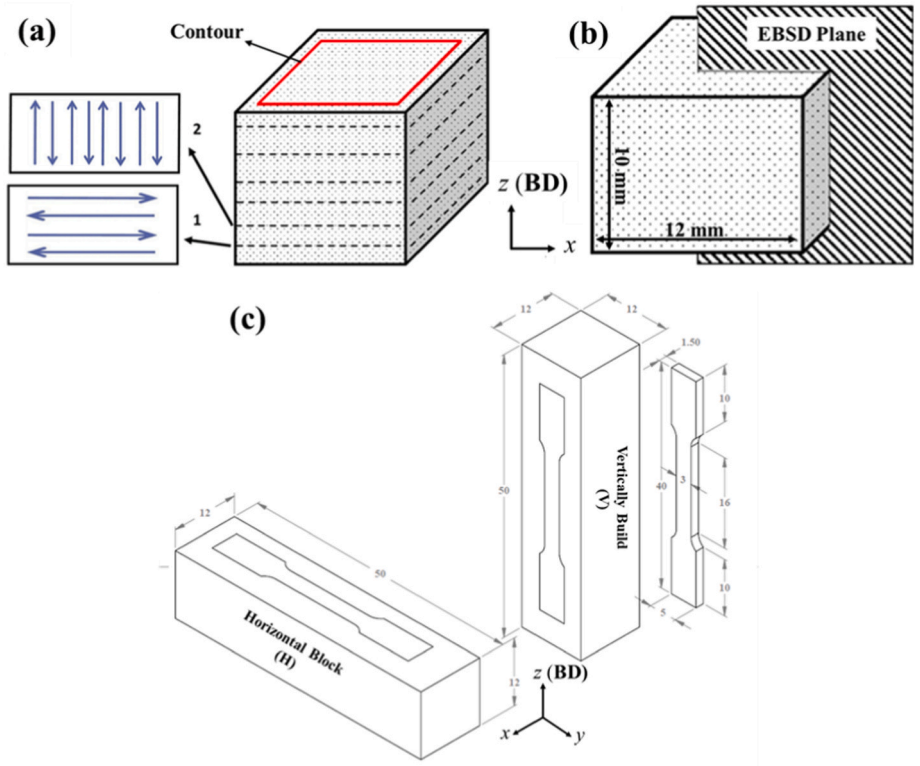

Fig. 2. Schematics showing (a) DED build process; (b) the observation plane for EBSD analysis; and (c) the tensile specimen extraction locations with respect to the DED fabricated sample blocks; all dimension units are in mm.

A video extensometer with a 100 mm axial field-of-view was used to measure the strain. At least three specimens were tested per condition to obtain the average tensile properties.

3. Results

3.1. Grain refinement

SEM micrographs of TiB_2 particles with characteristic size of $d_{90} = 1$ μm, $d_{90} = 10$ μm and $d_{90} = 40$ μm are shown in Fig. 3a, b and c, respectively. The corresponding micrographs of feedstock IN718 powders mixed with the TiB_2 powders are shown in Fig. 3d, e and f. Fig. 3d shows that the TiB_2 powders of $d_{90} = 1$ μm agglomerated during the ball milling and they were not evenly distributed over the surface of the IN718 powders. For the larger powder ($d_{90} = 40$ μm), TiB_2 did not attach to the IN718 powders, Fig. 3f. In contrast, the TiB_2 powders of $d_{90} = 10$ μm attached reasonably well to the IN718 powders (Fig. 3e), resulting in a uniform distribution of TiB_2 particles on the surface of the feedstock powder. Therefore, the TiB_2 powders with the characteristic size of $d_{90} = 10$ μm were chosen for the following study.

Fig. 4a and c represent the EBSD inverse-pole-figure (IPF) maps of the High and Low Energy samples. The grain size distribution was analysed to derive the area-weighted fraction (A_f) and the data are plotted in Fig. 4e. A_f represents the area occupied by a specific grain size range and 10 μm increments have been used to separate the grains. For example, the area-weighted fraction of grains with typical sizes of between 0 and 10 μm is calculated as follows:

$$A_{f(0-10)} = \frac{\Sigma(\text{Area of grains with size 0 μm – 10 μm})}{\text{Total Area}} \quad (1)$$

Large columnar grains with size of >300 μm (circle equivalent diameter) can be observed in both the High and Low Energy deposits. The High Energy IN718 microstructure exhibits a higher fraction with ~22% of the area occupied by columnar grains of >300 μm when compared to ~10% in the Low Energy IN718, Fig. 4e.

The {100} pole figure exhibits the highest MUD value of 7.9 in High Energy IN718 as opposed to 5.2 in the Low Energy IN718, Fig. 4b and d. Both the {111} and {110} pole figures have a relatively weak texture when compared to the {100}; henceforth the {100} pole figures are used throughout the work. The pole figures presented here are based on analysis of >3000 grains; hence, the texture interpretation is statistically significant.

EBSD IPF maps of the IN718/TiB_2 deposits are shown in Fig. 5a to f, with the corresponding pole figures illustrated at the bottom right corner of each IPF map. Fig. 5a, b and c show the EBSD IPF maps of High Energy IN718/TiB_2 deposits with TiB_2 content of 0.5 wt%, 1.5 wt% and 2.5 wt%, respectively. Corresponding images for the Low Energy IN718/TiB_2 are shown in Fig. 5d, e and f. The grain size distribution of High and Low Energy IN718/TiB_2 is shown in Fig. 5g and h, respectively, with the results of High and Low Energy IN718 included for the purpose of comparison. The lowest concentration of inoculant studied (0.5 wt%) did not induce grain refinement (Fig. 5a and d). For both the High and Low Energy IN718/TiB_2 deposits, significant grain refinement can be seen when the TiB_2 content is ≥ 1.5 wt % (Fig. 5b–c and Fig. 5e–f). Additionally, the {100} pole figures indicate that the texture in the High and Low Energy IN718/TiB_2 deposits becomes weaker with the TiB_2 addition of ≥1.5 wt%.

The grain size distributions in Fig. 5g and h show consistently higher area fraction of grains with size of <100 μm in both the High and Low Energy IN718/TiB_2 compared to the IN718 deposits. Fig. 6 compares the percentage area occupied by small grains (<20 μm) and large grains (>300 μm) for different TiB_2 contents. For the High Energy deposits, the TiB_2 content increased the area occupied by smaller grains (<20 μm), while the area occupied by the large grains (>300 μm) was reduced from ~22% to ~3%. The area occupied by small grains (<20 μm) increased from 4.6% to 45% in Low Energy IN718/TiB_2 deposits. The large grains (>300 μm) were completely avoided in Low Energy IN718/TiB_2 deposits when the TiB_2 content was ≥1.5 wt%. Therefore, the rest of the paper

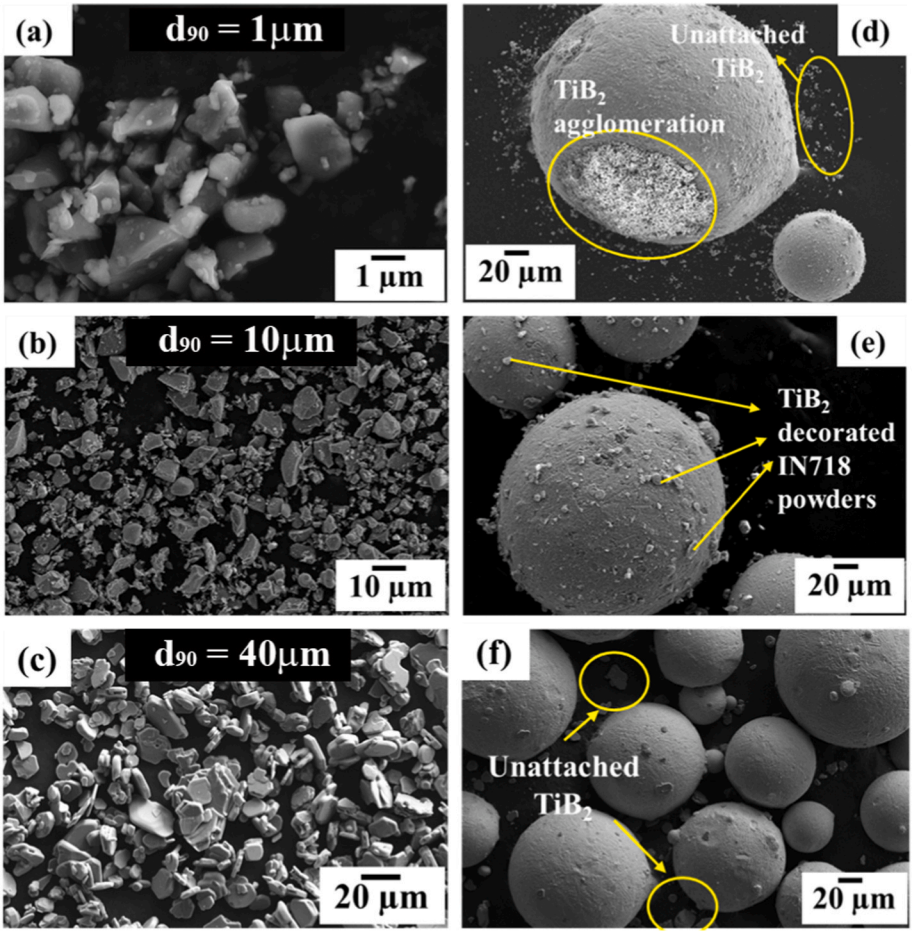

Fig. 3. TiB_2 powders with size of (a) $d_{90} = 1$ μm, (b) $d_{90} = 10$ μm and (c) $d_{90} = 40$ μm, respectively; the corresponding TiB_2 decorated feedstock powders with 1.5 wt % TiB_2 with particle size: (d) $d_{90} = 1$ μm (e) $d_{90} = 10$ μm (f) $d_{90} = 40$ μm.

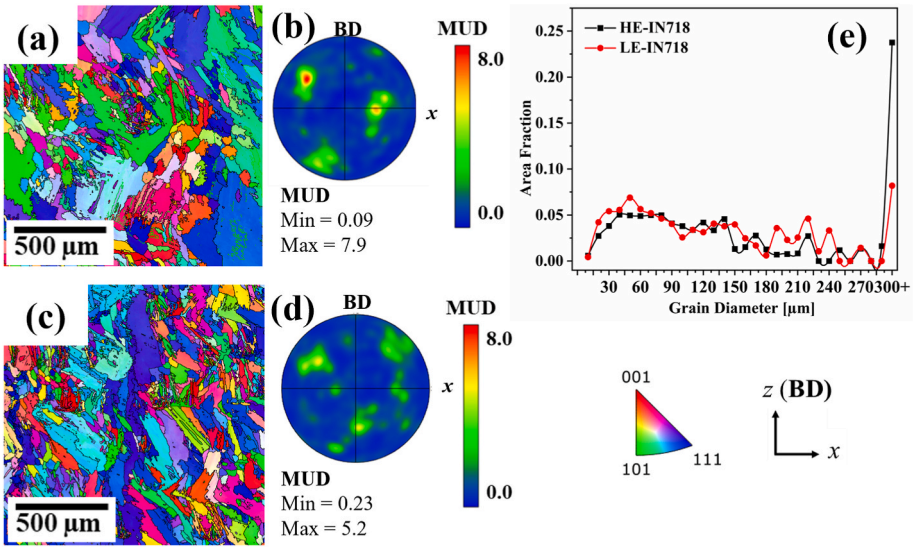

Fig. 4. As-deposited IN718 grain orientation maps and {100} pole figures: (a) and (b) for High Energy deposits; (c) and (d) for Low Energy deposits; (e) grain size distribution in High and Low Energy IN718 deposits.

focusses on the IN718/TiB_2 deposits with 1.5 wt% TiB_2, unless otherwise stated.

Unfortunately, the Low Energy IN718/TiB_2 deposits with TiB_2 content of ≥1.5 wt% and with powder flow rate of 12 g/min caused interlayer defects, as shown in Fig. 7a and b. The EDS point analysis (Point 1 in Fig. 7b) shows a high Ti peak (Fig. 7c), suggesting the presence of unmelted TiB_2 particles within the interlayer defects. In comparison, Ti peaks were not observed in the Low Energy IN718/TiB_2

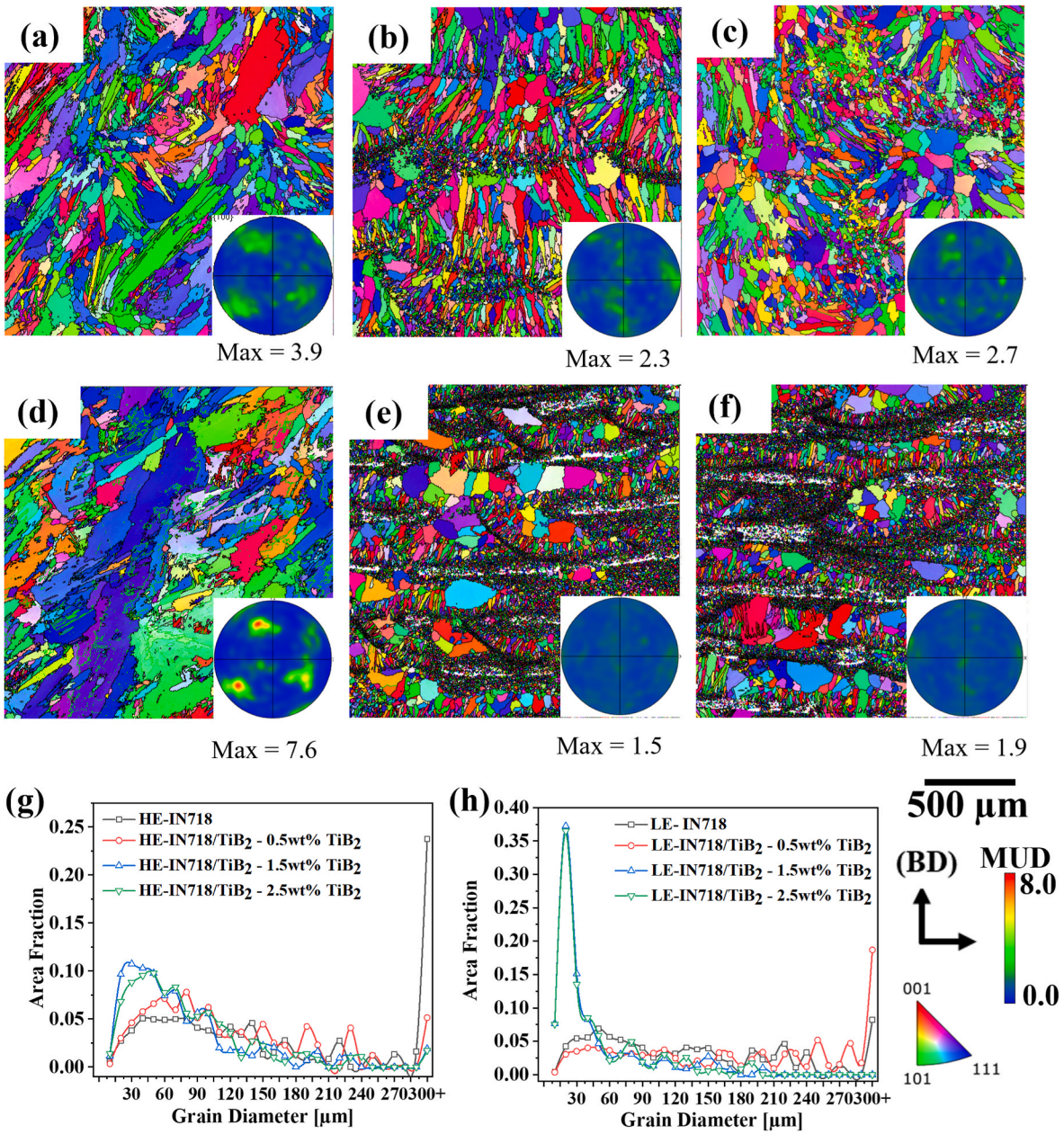

Fig. 5. EBSD maps of High Energy IN718/TiB_2 deposited with (a) 0.5 wt% (b) 1.5 wt% and (c) 2.5 wt% TiB_2; Low Energy IN718/TiB_2 deposited with (d) 0.5 wt% (e) 1.5 wt% and (f) 2.5 wt% TiB_2; (g) and (h) showing their grain size distributions. The inset of each IPF-BD map presents the corresponding {100} pole figures. HE: High Energy (E_l = 78.74 J/mm), LE: Low Energy (E_l = 33.08 J/mm).

matrix (Point 2 in Fig. 7b). The lower energy density likely results in the reduced melt pool temperature and thereby increased viscosity of the melt pool. A highly viscous melt pool reduces wettability, causing the melt to spheroidise and limiting its flow across the underlying surface [46]. This leads to interlayer pores and is generally referred to as the 'balling effect' [47]. Discontinuous scan tracks form due to the balling effect and large interlayer pores form as the next layer is deposited. Furthermore, the balling effect prevents the uniform deposition of the fresh powder on the previous layer, resulting in poor interlayer bonding. Therefore, it can be inferred that in the Low Energy IN718/TiB_2 deposits, the energy density was not sufficiently high to produce a melt pool with low viscosity to prevent the balling effect. This was the reason for the formation of interlayer defects.

Instead of increasing the linear energy density via changing laser power or scan speed, an alternative method was adopted in the present work to improve the densification in the Low Energy IN718/TiB_2. Here the powder flow rate was reduced from 12 g/min to 6 g/min, while keeping all other parameters the same. Thus, an unchanged linear energy density enabled comparison with Low Energy IN718. Upon reducing the flow rate, the number of powder particles fed in the melt pool per unit time is expected to be lower. By doing so, the laser energy experienced by individual powders should be higher, which helped to reduce the viscosity of the melt pool.

Fig. 8a–f show SEM micrographs and corresponding EBSD IPF maps of the Low Energy IN718/TiB_2 deposits using powder flow rate of 8 g/min, 7 g/min and 6 g/min. Fig. 8g and h show plots revealing the effect of powder flow rate on the grain size distribution and area percentage of defects. The deposit with a flow rate of 12 g/min exhibited ~2.5% defects, which decreased to <1.0% at a flow rate of 8 g/min (Fig. 8h). A fully dense deposit without interlayer defects was achieved with a flow rate of 7 g/min and below (Fig. 8b and c). Therefore, all the following Low Energy IN718/TiB_2 deposits were produced with a flow rate of 7 g/

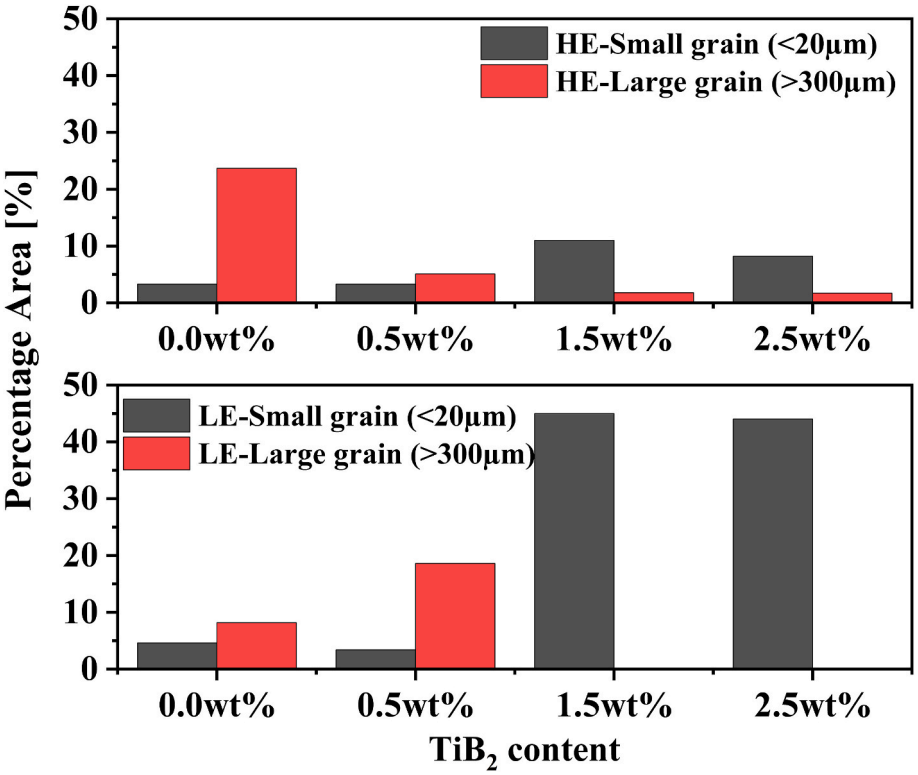

Fig. 6. Percentage of total grain area occupied by small grains (<20 μm) and large grains (>300 μm) in IN718 and IN718/TiB_2 deposits. HE: High Energy (E_l = 78.74 J/mm), LE: Low Energy (E_l = 33.08 J/mm).

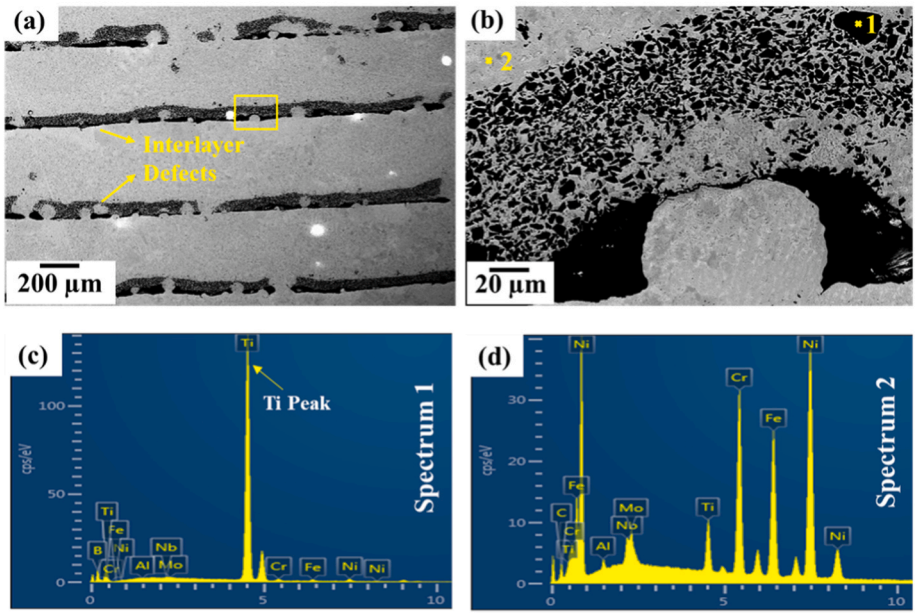

Fig. 7. (a) Low Energy IN718/TiB_2 deposits with 1.5 wt% TiB_2 and flow rate of 12 g/min having interlayer defects; (b) a higher magnification view showing the EDS points; (c) the corresponding EDS spectrum of point 1 showing unmelted particles exhibiting sharp Ti peak in comparison with (b) EDS spectrum of the IN718/TiB_2 matrix as collected from point 2.

min to achieve the desired densification, unless otherwise stated. The IPF maps in Fig. 8e and f show that grains became coarser as the flow rate was reduced below 8 g/min. The area fraction of the small grains (<20 μm) decreased with the decreasing flow rate, which was accompanied by the higher fraction of grains with size of >100 μm, Fig. 8g.

3.2. Phase evolution

The detailed microstructure of IN718 is compared with IN718/TiB_2 in Fig. 9a–e, and micro-hardness is compared in Fig. 9f. Both the High and Low Energy IN718 deposits contain an inter-dendritic network of Laves phase, as revealed by the bright contrast phase in Fig. 9a and c, which is typical of AM IN718 [3,4]. Laves phase is formed as a result of

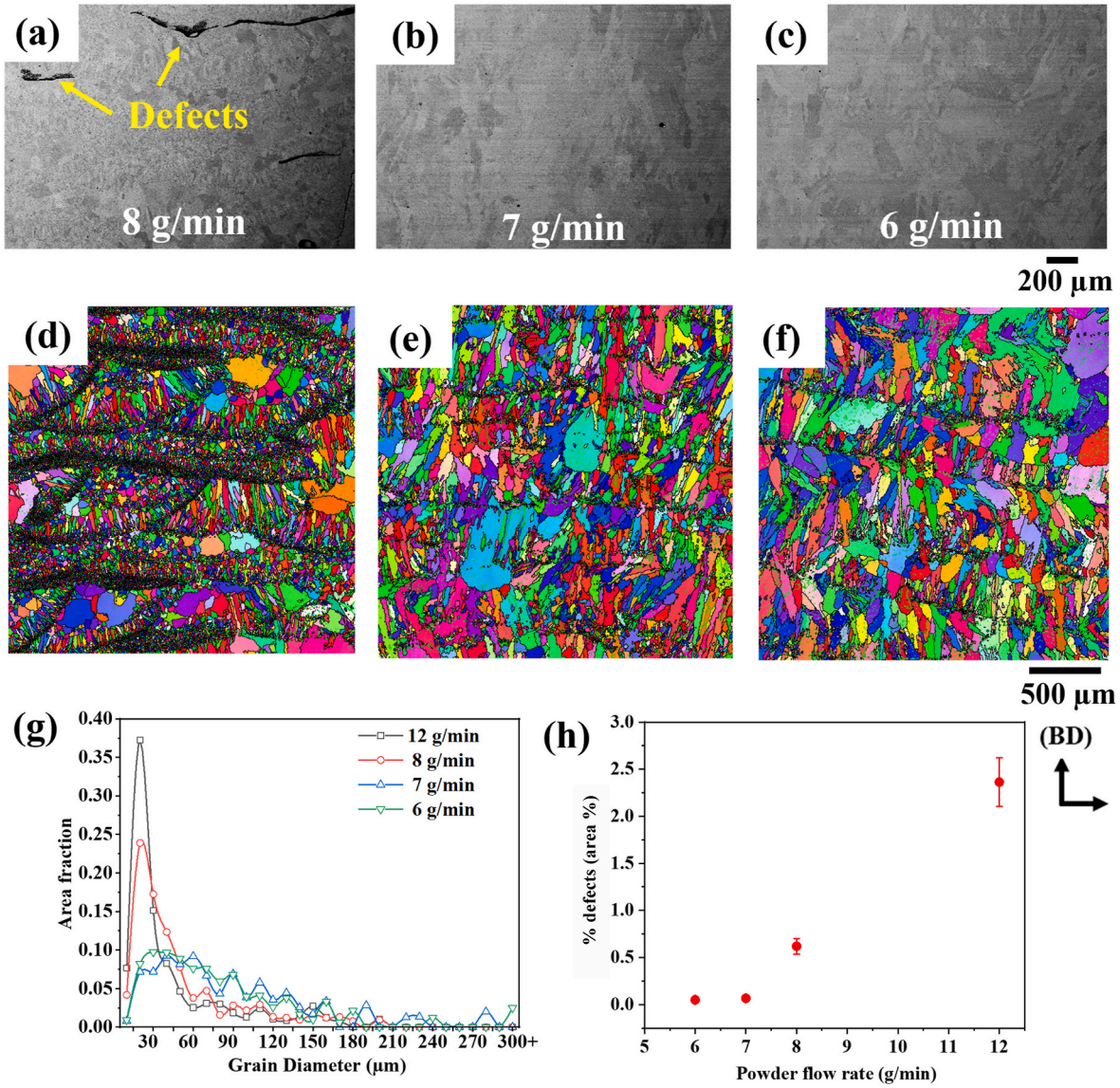

Fig. 8. SEM micrographs and EBSD IPF maps of Low Energy IN718/TiB_2 deposits produced with varying powder flow rate: (a) and (d) 8 g/min; (b) and (e) 7 g/min; (c) and (f) 6 g/min; and plots showing the effect of powder flow rate on the grain size distribution (g) and area percentage of porosities (h). All the deposits were processed with a TiB_2 content of 1.5 wt%.

rapid solidification where elements, such as Nb and Mo with low partition coefficient, segregate to the last remaining liquid in the inter-dendritic region. It is known that the Laves phase is detrimental to tensile ductility of IN718 [2]. The microstructure of High and Low Energy IN718/TiB_2 as shown in Fig. 9b and d illustrates that the inter-dendritic 'bright' Laves phase as observed in the IN718 (Fig. 9a and c) is vastly reduced in terms of its size and area fraction. The reduced fraction of Laves phase particles was accompanied with the presence of needle-shaped and spherical precipitates in IN718/TiB_2. Fig. 9e shows that these precipitates are distributed evenly within the matrix. The needle-shaped precipitates with a mean aspect ratio of ~3.5 have an area fraction of ~10% for the High Energy IN718/TiB_2, which is reduced to ~5% in the Low Energy IN718/TiB_2. By comparison, the spherical precipitates have <1% area fraction for both the High and Low Energy IN718/TiB_2. Overall, TiB_2 addition leads to a significant hardness increase from ~250 Hv in as-deposit IN718 (both Low and High Energy) to ~500 Hv in High Energy IN718/TiB_2, and ~400 Hv in Low Energy IN718/TiB_2 deposits, Fig. 9f. The lower content of the needle-shaped precipitates in the Low Energy IN718/TiB_2 is correlated to the lower hardness when compared to the High Energy IN718/TiB_2.

Fig. 10a and b show the EDS elemental maps of the High and Low Energy IN718/TiB_2, respectively. The needle-shaped precipitates are rich in Cr, Mo, Nb and B elements, while there is Ti enrichment in the spherical precipitates. Similar observation was revealed by performing an EDS line scan, with the representative results given in Fig. 10c–e. The needle-shaped precipitate (Fig. 10d) exhibits Cr, Mo and Nb peaks, while a high Ti concentration is shown for the spherical precipitate (Fig. 10e).

Fig. 11 compares the XRD spectra of High and Low Energy IN718/TiB_2 deposits as well as the High Energy IN718 deposit. The strong diffraction peaks corresponding to the face-centred-cubic (FCC) γ-phase are readily indexed for both the High and Low Energy IN718/TiB_2 deposits. For the IN718 deposit peaks of Laves phase are observed, which is consistent with literature data [48]. These peaks are absent in both the High and Low Energy IN718/TiB_2. This finding correlates with the reduced Laves phase as revealed by SEM imaging of Fig. 9a–e. Moreover, the High and Low Energy IN718/TiB_2 deposits exhibit peaks indicating both the Cr_3B_4 and TiB_2 phases (JCPDS database [04-003-6119] and [00-035-0741]). The TiB_2 has a high peak intensity at the 2θ angle overlapping with the γ matrix; therefore, two characteristic peaks at 2θ angles of ~26° and ~35° were used to index the TiB_2 phase (see the

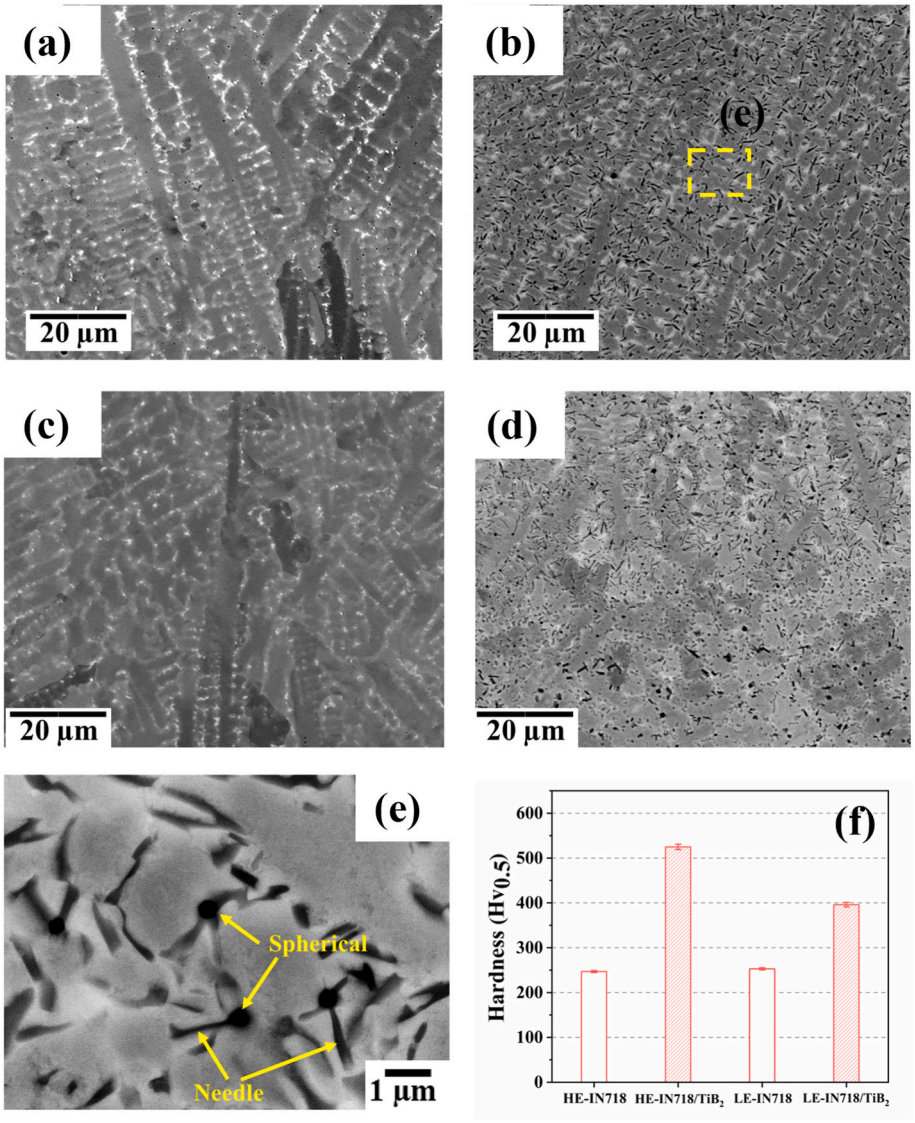

Fig. 9. SEM images showing typical microstructures of IN718 with and without inoculants: (a) High Energy IN718; (b) High Energy IN718/TiB_2; (c) Low Energy IN718 and (d) Low Energy IN718/TiB_2; (e) high-magnification image of the High Energy IN718/TiB_2 deposit showing the needle-shaped and spherical precipitates; (f) comparison of the average hardness values. HE: High Energy (E_l = 78.74 J/mm). LE: Low Energy (E_l = 33.08 J/mm).

figure inset). The presence of Cr_3B_4 peaks agrees well with the EDS elemental maps in Fig. 10a and b, in terms of showing the Cr and B rich needle-shaped precipitates in the IN718/TiB_2 deposits. The XRD peaks of TiB_2 confirm that the Ti-rich spherical precipitates, as shown in Fig. 10c, are the TiB_2 particles that survived in the melt, having a reduced size.

3.3. Tensile properties

Representative engineering stress-strain curves for the DED IN718 and IN718/TiB_2 deposits using both the High and Low Energy process parameters are shown in Fig. 12a and c. For each sample condition, tensile tests were performed parallel (vertical: V) and perpendicular (horizontal: H) to the build direction to allow evaluation of the property anisotropy. Fig. 12b and d present the data in bar charts to aid comparison of the yield strength, tensile strength, and elongation-to-failure. The bar charts represent the average values obtained from at least three tests per condition. Overall, there was a significant improvement in terms of the material strength in the IN718/TiB_2 deposits in comparison with the IN718 alone; however, the ductility was drastically reduced. The material strength of IN718/TiB_2 is comparable to the solution treated and aged DED IN718 [49].

Tensile strength and yield strength of the High Energy IN718-(V) specimens (i.e., parallel to the build direction) were higher than those of the High Energy IN718-(H) specimens (i.e., perpendicular to the build direction), Fig. 12a. In contrast, tensile ductility had the opposite trend, with the average elongation-to-failure of ~28% for the High Energy IN718-(H), while ~16% for the High Energy IN718-(V), Fig. 12b. Addition of TiB_2 as an inoculant in the DED IN718 caused a yield strength increase ~400 MPa for the High Energy IN718/TiB_2-(V) and ~300 MPa for the High Energy IN718/TiB_2-(H), respectively, but at a cost of tensile ductility, Fig. 12a. The elongation-to-failure reduced to ~3% in the High Energy IN718/TiB_2-(V) and ~5% for the High Energy IN718/TiB_2-(H) specimens, Fig. 12b, which represents a significant ductility reduction when compared to the sample build without the TiB_2 addition.

For the Low Energy deposits, yield strength and tensile strength of Low Energy IN718-(H) specimens were higher than those of the Low Energy IN718-(V) specimens. However, the tensile ductility had marginal difference between the two test directions. An increase of ~500 MPa and ~400 MPa of the yield strength was observed in the Low Energy IN718/TiB2-(V) and Low Energy IN718/TiB2-(H) specimens,

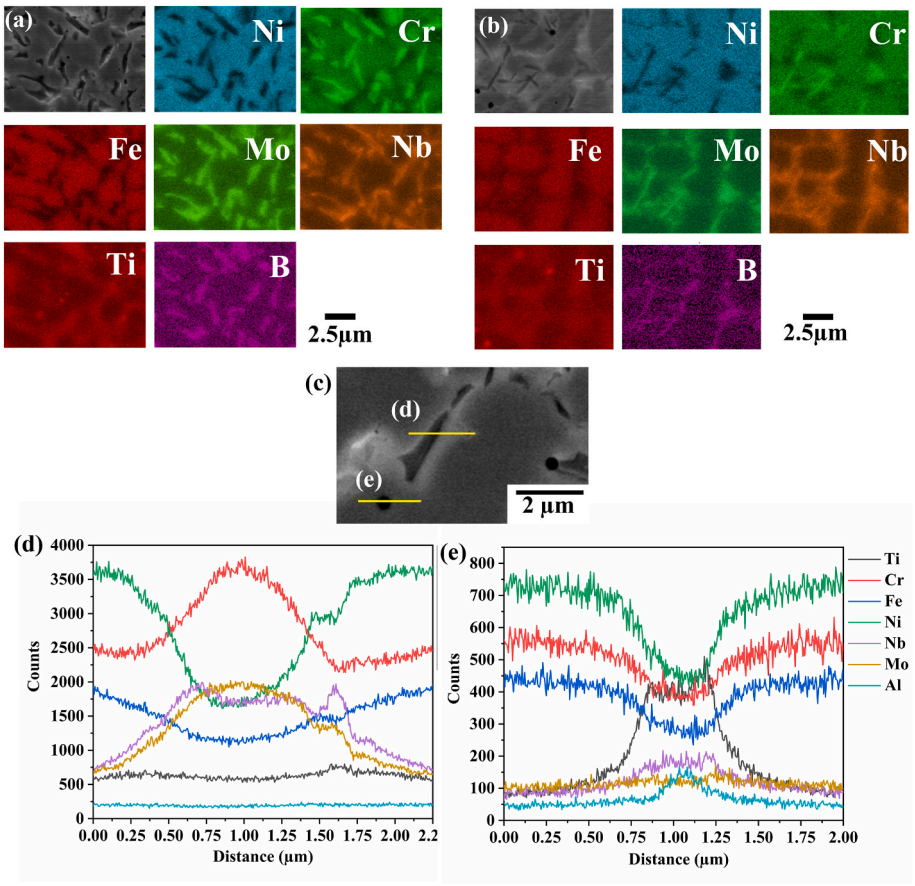

Fig. 10. EDS elemental map for (a) High Energy IN718/TiB_2, (b) Low Energy IN718/TiB_2 deposits; (c) EDS line scan of LE-IN718/TiB_2 deposit showing segregation of Cr, Mo, Nb and B at the needle-shaped precipitate in (d) and Ti segregation at the spherical precipitate in (e).

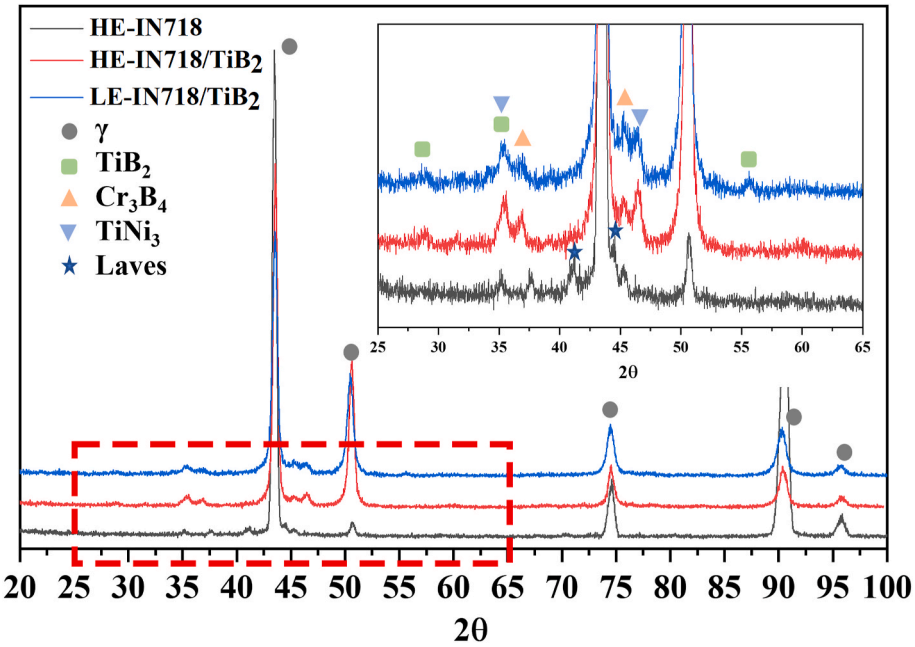

Fig. 11. Comparison of the XRD spectra collected from the DED IN718 and IN718/TiB_2 in both the High and Low Energy conditions. Figure inset is the enlarged view with diffraction angles ranging from 25° to 65°. HE: High Energy (E_l = 78.74 J/mm). LE: Low Energy (E_l = 33.08 J/mm).

respectively, compared to the respective Low Energy IN718 specimens. A significant drop in ductility due to the TiB_2 addition was noted as represented by the reduced elongation-to-failure ~2% for both the Low Energy IN718/TiB_2-(V) and Low Energy IN718/TiB_2-(H) specimens, (Fig. 12b).

Fig. 13a–i summarises the key observations of the SEM cross-

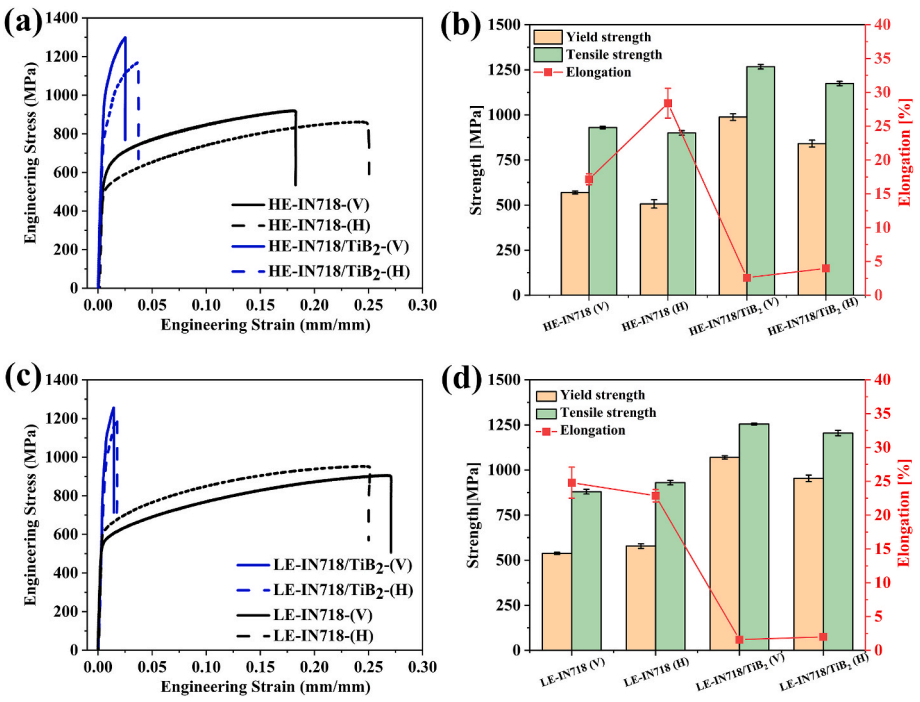

Fig. 12. Engineering stress-strain curves for IN718 and IN718/TiB_2 deposits tested in vertical (V) and horizontal (H) directions for (a) High Energy and (c) Low Energy deposits. The average value of yield strength, tensile strength, and the elongation-to-fracture for each sample condition are summarised in (b) High Energy and (d) Low Energy deposits. HE: High Energy (E_l = 78.74 J/mm). LE: Low Energy (E_l = 33.08 J/mm).

sectional view of the tensile fractured surface and the corresponding SEM fractography. In terms of the IN718 deposit, micro-cracks were frequently observed at the interface between the inter-dendritic Laves phase and the IN718 matrix (Fig. 13a and d, as well as their enlarged views in 13 b and Fig. 13e). By contrast, for the IN718/TiB_2, a high density of micro-cracks appeared near the interface of the matrix and the needle–shaped precipitates (Fig. 13g and j), as well as their enlarged views in Fig. 13h and k). The high loads generated due to the strengthening effect of these needle–shaped precipitates were too high to be accommodated by the IN718 matrix. As a result, this led to the micro-crack initiation at the interface as indicated by arrows in Fig. 13h and k. The high density of micro-cracks is the likely cause of early failure in IN718/TiB_2. For both the IN718 and IN718/TiB_2 materials, the SEM fractography reveals typical ductile dimples. Occasionally, unmelted particles (possibly TiB_2) were observed on the fracture surface.

4. Discussion

4.1. TiB_2 as an inoculant for DED IN718

The present investigation demonstrates significant grain refinement (Fig. 5a–h) and strengthening (Fig. 12a–d) in the IN718/TiB_2 deposits (both High and Low Energy) compared to the corresponding IN718 deposits. However, the secondary phases in IN718/TiB_2 were significantly different from IN718 (Fig. 9a–e), suggesting a differing solidification sequence. The general solidification sequence of IN718 starts with formation of γ from the liquid (L → L + γ) and the solidification process terminates with the formation of γ + Laves eutectic [50–52]. During solidification, elements such as Nb, Mo and C can segregate, with Nb having the lowest elemental partitioning coefficient of $k < 0.5$; thus, the formation of Laves phase in the last solidified inter-dendritic region [53]. The presence of Laves phase is detrimental to tensile ductility in DED and L-PBF IN718 via micro-crack initiation and propagation [3,9]. Moreover, due to high cooling rates, the precipitation of γ′ and γ″ is suppressed in the as-built DED IN718 [12]. TiB_2 addition seems to alter the solidification path, causing the formation of fine and distributed Cr-, Mo-, Nb- and B-enriched needle-shaped precipitates as opposed to the network of inter-dendritic Laves phase, Fig. 10a–e. These needle-shaped precipitates, along with the spherical TiB_2, facilitate grain refinement in the IN718/TiB_2 deposit and also help to preven the formation of an inter-dendritic Nb-rich Laves phase network by reducing the available Nb, Mo required for the Laves phase formation (Fig. 9a and c).

The microstructural evolution from the premixed IN718/TiB_2 powder to the bulk DED deposited material is illustrated by schematic diagrams in Fig. 14a – Fig. 14c. The TiB_2 particles are distributed evenly on the surface of feedstock IN718 powders after the ball milling (Fig. 14a). During the DED process, the high-temperature melt pool leads to the full or partial dissolution of the TiB_2 particles, Fig. 14b and c. This agrees well with the SEM observation as shown in Fig. 10c and e, revealing the presence of Ti-rich spherical precipitates in the IN718/TiB_2, and also with the XRD-based phase analysis (Fig. 11). For low TiB_2 addition (0.5 wt%), the TiB_2 particles were almost all dissolved during the DED process, and the microstructure of the IN718/TiB_2 sample resembles that of IN718 (Fig. 14d vs. Fig. 9a). For the higher TiB_2 content (Fig. 14e and f), where the TiB_2 particles were able to survive in the melt, the number density of the needle-shaped and spherical precipitates was significantly higher.

The TiB_2 addition primarily results in the formation of needle-shaped precipitates rich in Cr, Nb, Mo and B, along with the lesser amount of Ti and B enriched spherical precipitates. These precipitates act as the heterogeneous grain nucleation sites, resulting in the refined microstructure and improved material strength. To generate effective grain refinement, there is a need to ensure the minimum TiB_2 addition, which is 1.5 wt% for the present DED IN718/TiB_2 deposits (both High and Low Energy). No further grain refinement was achieved when the TiB_2 content was increased from 1.5 wt% to 2.5 wt%. A similar observation was reported by Matysiak et al. [54] who investigated the effect of inoculant ($CoAl_2O_4$) concentration on the grain size of cast IN713C Ni-base superalloy. Significant grain refinement was observed upon using 5 wt% inoculant. However, when increasing the inoculant concentration from 5 wt% to 10 wt%, only a minor improvement was noted. Agglomeration of the inoculant particles was found to be detrimental for the potency of

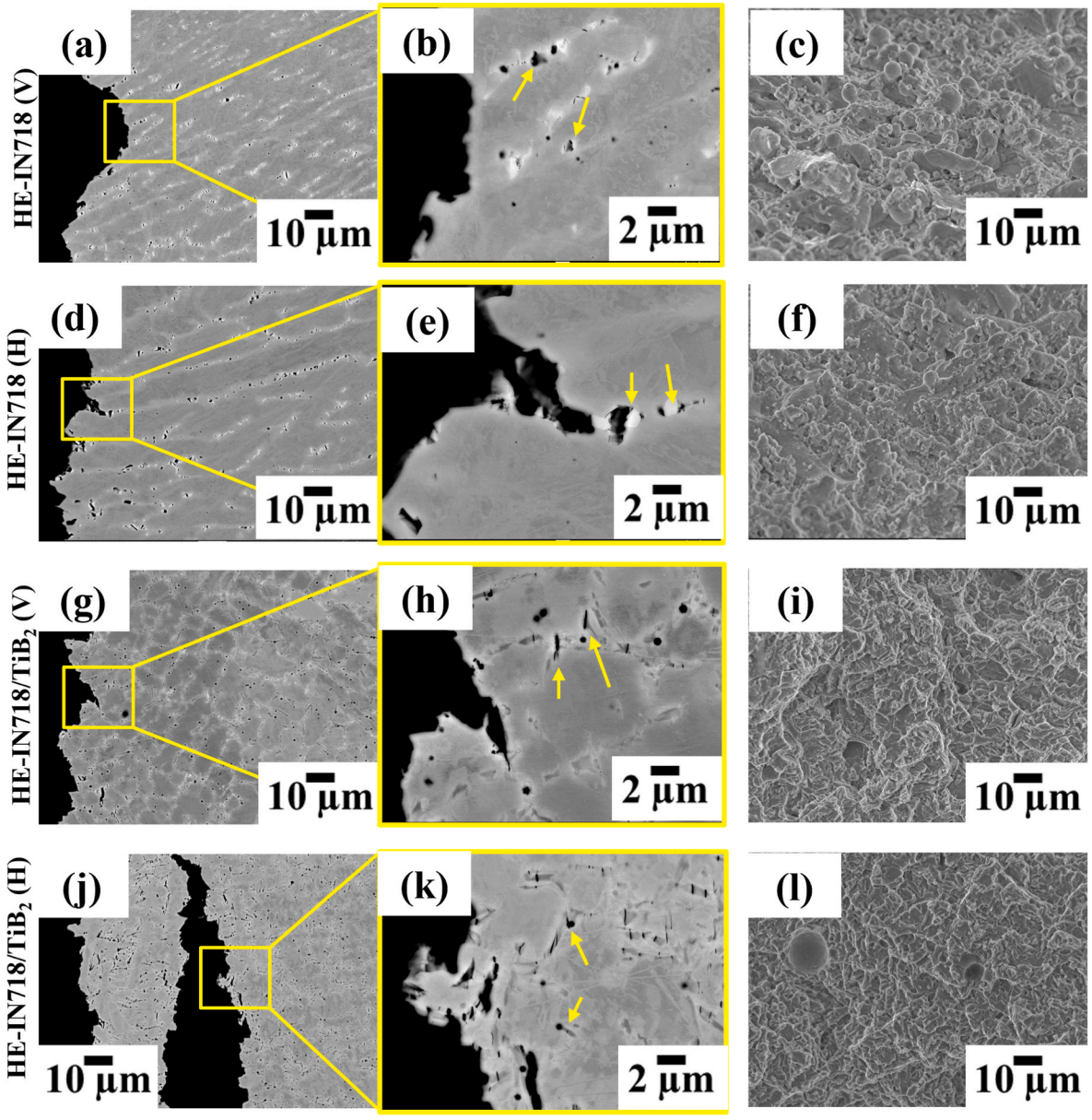

Fig. 13. SEM cross-sectional view of the fracture surface and SEM fractography: (a), (b) and (c) High Energy IN718-(V); (d), (e) and (f) High Energy IN718-(H); (g), (h) and (i) High Energy IN718/TiB_2-(V); (j), (k) and (l) High Energy IN718/TiB_2-(H). Micro-porosity arising from separation of Laves phase from the matrix in IN718 and separation of the needle-shaped and spherical precipitates from matrix in IN718/TiB_2 are indicated by arrows. HE: High Energy (E_l = 78.74 J/mm).

the inoculants in providing grain refinement [55]. Liu et al. [56] and Yang et al. [57] observed that the potency of the inoculant particles as grain refiner reduced after reaching a critical value. In both studies, the authors related the reduced efficiency to the particle agglomeration. It is possible that TiB_2 powder addition in the present study caused agglomeration of the TiB_2 particles, and thereby limiting their role on effective grain refinement. Moreover, the latent heat evolution during the growth could have prevented further undercooling and nucleation, consistent with the work of Spittle et al. [58], who studied the role of inoculant on grain refinement in Al alloys. However, further work is required to provide a definite answer.

4.2. Strengthening mechanisms and strength comparison with literature data

The strengthening mechanisms of metal matrix composites that has been widely accepted in the literature are: 1) grain boundary strengthening ($\sigma_{Hall-Petch}$) [40,59]; 2) dislocation strengthening (σ_{GND}) [60,61]; 3) Orowan strengthening (σ_{Orowan}) [62,63]; and 4) load transfer effect (σ_{load}) [59,61]. In this section, we have explored the possible strengthening mechanisms in high-energy IN718/TiB_2 in comparison to high-energy IN718 deposits.

Grain boundaries can hinder movement of dislocations; thus, increase material strength. The Hall–Petch effect [64] is a very well-known strengthening mechanism that relates grain size to strength, described as follows:

$$\sigma_{Hall-Petch} = \sigma_0 + k_y d^{-1/2} \tag{2}$$

where σ_0 and k_y are material constants, and d is the grain size. According to the EBSD results (Figs. 4 and 5), the average grain size reduced from 31.4 µm to 23.8 µm as a result of TiB_2 addition. The increase in yield strength due to grain refinement ($\Delta\sigma_{Hall-Petch}$) in the IN718/$TiB_2$ deposit is estimated using Eq. (3) [40,59,60]:

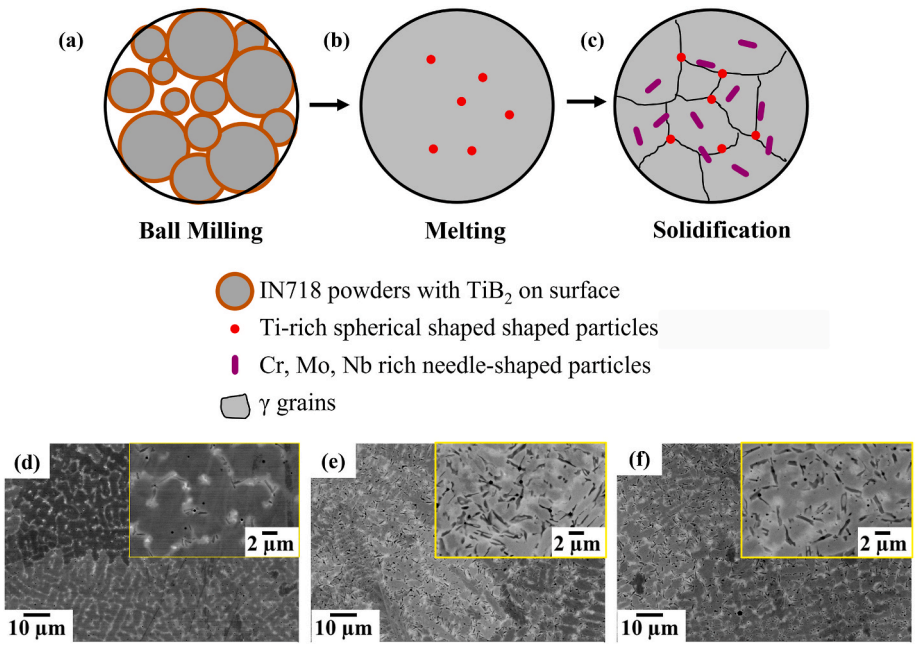

Fig. 14. Schematic diagrams showing the effect of TiB_2 on the solidification path: (a) ball milling, (b) melting and (c) solidification; SEM micrographs for High Energy-IN718/TiB_2 with TiB_2 content (d) 0.5 wt%, (e) 1.5 wt% and (f) 2.5 wt%.

$$\Delta\sigma_{Hall-Petch} = k_y\left(d_{IN718}^{-\frac{1}{2}} - d_{IN718/TiB_2}^{-\frac{1}{2}}\right) \tag{3}$$

The value of k_y was reported as 1260 MPa$\sqrt{\mu m}$ in Refs. [65,66] and 750 MPa$\sqrt{\mu m}$ [40,67] for IN718. Thus, the upper and lower limits for the strength increment due to grain size reduction are estimated as ~35 MPa and ~20 MPa, respectively.

For MMCs, residual plastic strain is caused by the difference in the coefficients of thermal expansion (CTE) between the matrix and particles and results in the increase in geometrically necessary dislocations (GNDs) [25,61]. The contribution of GNDs to yield strength can be calculated using the following expression [40,60]:

$$\sigma_{GND} = \beta Gb\left(\sqrt{\rho_{GND}}\right) \tag{4}$$

where G and b are the shear modulus and the length of Burgers vector of the IN718 matrix. Values of G = 76.9 GPa and b = 0.26 nm were reported in Ref. [68]. β is a constant with value of 1.25 for IN718 from Kong et al. [40]on L-PBF IN718. Using Eq. (5), which compares the IN718/TiB_2 with the IN718 alone, the strengthening effect due to additional GNDs as observed in the IN718/TiB_2 deposit can be evaluated:

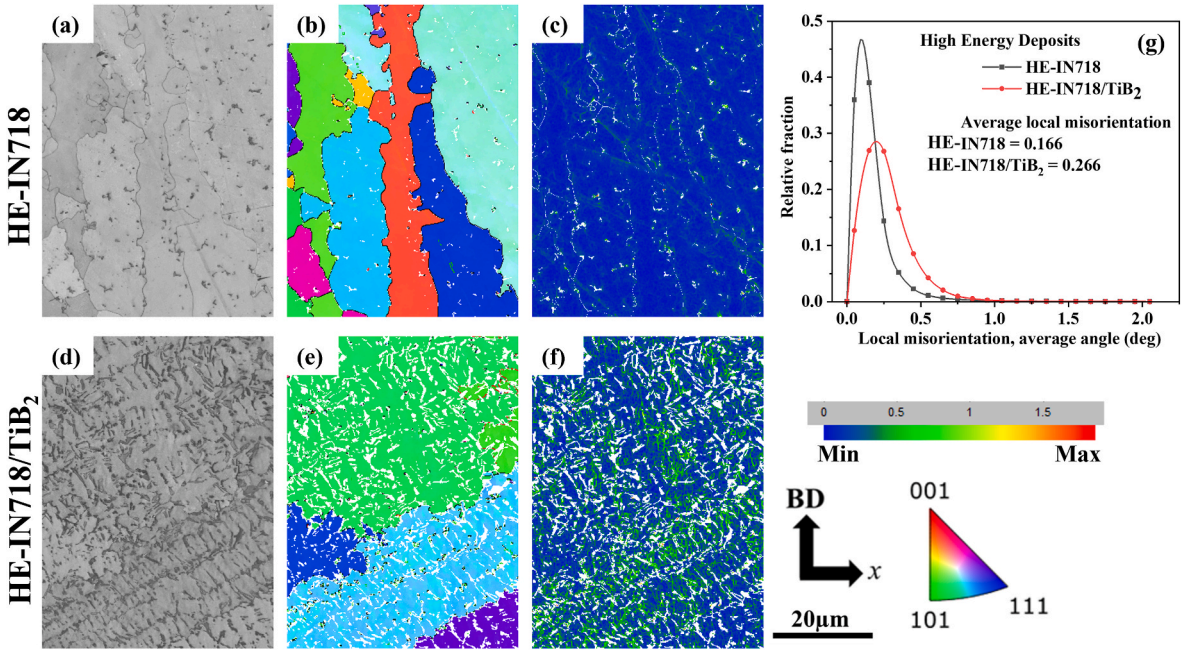

Fig. 15. EBSD maps for High Energy deposits: (a) and (d) band contrast maps; (b) and (e) IPF maps; (c) and (f) local misorientation maps for High Energy-IN718 and High Energy-IN718/TiB_2, respectively; (g) comparison of the local misorientation distributions. HE: High Energy (E_l = 78.74 J/mm).

$$\Delta\sigma_{GND} = \sigma_{GND}^{IN718/TiB_2} - \sigma_{GND}^{IN718} \quad (5)$$

ρ_{GND} in Eq. (4) denotes the density of GNDs as estimated from the EBSD local area misorientation map. For constructing the local area misorientation maps, EBSD scans were performed using a fine step size of 0.15 μm. The local misorientation maps for the IN718 and IN718/TiB_2 deposits are shown in Fig. 15c and f. The respective band contrast and IPF maps are shown in Fig. 15a and b for IN718, while Fig. 15d and e display those for IN718/TiB_2. Fig. 15g compares the distribution of the local misorientations between the two conditions, i.e., with and without the TiB_2 addition.

The average value of the local misorientation increased from 0.164° to 0.266°, Fig. 15g, indicating a significant difference between the IN718/TiB_2 and IN718 deposits (Fig. 15f vs. Fig. 15c). It is also evident that the high local misorientation region coincides with the secondary phases in the IN718/TiB_2 deposits (comparing Fig. 15d and f), indicating the local lattice distortion in the vicinity of the precipitates. Therefore, it can be inferred that the micro-segregation due to TiB_2 addition led to increased GNDs in the IN718/TiB_2 deposits. The GND density was calculated from the average misorientation angle using Eq. (6) [69]:

$$\rho_{GND} = \frac{a\theta}{bu} \quad (6)$$

where θ is the average value of local misorientation, and a is a constant with a value of 3 [69,70]. u is the distance between the misoriented points which is the "step size" of the EBSD map. It is important to note that, unlike geometrically necessary dislocations (GNDs), the statistically stored dislocations (SSDs) do not produce observable lattice curvature, rendering them indiscernible through EBSD measurements [69]. Therefore, GND density based on EBSD measurements were used in our calculation. Similar approach of using EBSD measurements to estimate the increased dislocation density due to the CTE mismatch was performed by AlMangour et al. [25] on SLM processed TiB_2 strengthened 316L stainless steel. Using Eq (6) the value of ρ_{GND} was calculated as $\sim 3.65 \times 10^{14}\ m^{-2}$ for IN718/TiB_2 deposits, which is higher than $\sim 2.25 \times 10^{14}\ m^{-2}$ for the IN718 deposit. The contribution of increased GNDs to the strength increment of IN718/TiB_2 ($\Delta\sigma_{GND}$) is thus estimated to be ~100 MPa using Eq (5).

The needle-shaped precipitates in IN718/TiB_2, as observed in Fig. 9b and d can produce a pinning effect on dislocation motion, and additional shear stress is needed to allow dislocations to by-pass the precipitates. This is the Orowan strengthening effect, and its contribution to the material strength can be estimated using Eq (7) [61,71,72].

$$\Delta\sigma_{Orowan} = \frac{0.4GbM}{\pi(1-\nu)^{\frac{1}{2}}\lambda} ln\frac{\sqrt{\frac{2}{3}}d_p}{b} \quad (7)$$

$\nu = 0.28$ is Poisson's ratio, and λ is the interparticle spacing with the value calculated to be 595 nm using Eq (8) [40,72]:

$$\lambda = \sqrt{\frac{2}{3}}d_p\left(\sqrt{\frac{\pi}{4V_p}} - 1\right) \quad (8)$$

where d_p is the average particle diameter, and V_p is the volume fraction of the needle-shaped precipitates. The values of d_p and V_p was determined as 289 nm and 0.11, respectively. To determine the values of d_p and V_p, measurements were performed on 4–6 SEM images like the one shown in Fig. 9e, and the d_p value was measured by considering the average width of the needle-shaped precipitates. The yield strength increment due to Orowan strengthening mechanism is estimated as ~106 MPa.

Load transfer effect is another common strengthening mechanism in MMCs. The strong interfacial bonding between the secondary phase and matrix can contribute to the transfer of the load applied from the soft matrix to the hard reinforcements. Assuming well-bonded and spherical particles for simplicity, the contribution of load transfer effect to the strengthening of IN718/TiB_2 can be represented as [40,61,62]:

$$\Delta\sigma_{load} = 0.5V_p\sigma_m \quad (9)$$

where $V_p = 0.11$ is the volume fraction of the strengthening particles and σ_m is the yield strength of the matrix, and its value is considered to be the same as the yield strength of the IN718. Thus, the contribution of $\Delta\sigma_{load}$ to the strengthening of IN718/TiB_2 is estimated as ~30 MPa.

TiB_2 addition to IN718 processed by DED results in substantial improvement of hardness (Fig. 9f) and tensile strength (Fig. 12). The overall contribution of all these strengthening mechanisms towards the increment of yield strength ($\Delta\sigma$) at room temperature can be obtained using the summation method [24,40]. This approach is commonly utilized to analyse the increase in yield strength of metal matrix composites, considering different strengthening mechanisms. For instance, Kong et al. [40] applied this method to analyse the yield strength enhancement in IN718 alloy strengthened with $TiAl_2C$ fabricated using DED. Similarly, Wang et al. [60] and Li et al. [24] employed this technique to study the yield strength improvement in 316L stainless steel reinforced with TiN and AlSi10Mg alloys reinforced with TiB_2, respectively, both processed through LPBF. The summation method predicts the strength of metal matrix composites using simple arithmetic sum, assuming the individual strengthening mechanisms to be independent, as shown in Eq (10).

$$\Delta\sigma = \Delta\sigma_{Hall-Petch} + \Delta\sigma_{GND} + \Delta\sigma_{Orowan} + \Delta\sigma_{load} \quad (10)$$

The value of Δσ was calculated as ~260 MPa, which is lower than the yield strength difference of the IN718 and IN718/TiB_2, as measured experimentally (Fig. 12b), ~400 MPa with loading axis parallel to build direction, and ~300 MPa with loading axis perpendicular to build direction. Hence, the strengthening mechanisms considered in this section do not account for actual strength increment in IN718/TiB_2. It is possible that other strengthening mechanism(s), such as grain boundary strengthening by Boron, solid solution strengthening is contributing to the increased strength in IN718/TiB_2, that is hard to analytically account for or to quantify using the characterisation techniques employed in the current investigation. In their study, Kontis et al. [73] employed atom probe tomography (APT) and high-resolution secondary ion mass spectroscopy (SIMS) to investigate the grain boundary nature of polycrystalline superalloy due to Boron addition. Their findings revealed a uniform dispersion of boride particles along the grain boundaries, contributing to enhanced creep resistance in the examined superalloy. Furthermore, the ongoing investigation considers solely the contribution of geometrically necessary dislocations (GNDs). A more comprehensive assessment of the yield strength enhancement due to the addition of TiB_2 could potentially be achieved by incorporating the total dislocation density, considering both geometrically necessary dislocations (GNDs) and statistically stored dislocations (SSDs). Therefore, further investigation is needed for determining the strengthening mechanism of IN718/TiB_2. Moreover, the current investigation explores the mechanical properties of IN718 and IN718/TiB_2 in the as-deposited condition. Therefore, the effect of coherent strengthening effect due to the γ' and γ'' precipitates have not been explored.

There exist several other models for predicting the yield strength increment in metal matrix composites combining the impact of these strengthening mechanisms. The Clyne model [61] predicts the yield strength by employing a root mean square method to combine the strengthening mechanisms, assuming interdependence among them. The Ramakrishnan model [74] incorporates the increased dislocation density due to thermal mismatch and load transfer effects caused by reinforcement particles to predict yield strength. The Zhang and Chen [63] model further builds upon the Ramakrishnan model by incorporating the effects of Orowan strengthening, load transfer effects, and dislocation strengthening to predict the yield strength of MMCs.

Sahoo et al. [2], conducted a comprehensive comparison of different yield strength prediction models to interpret the mechanisms behind the

enhanced yield strength observed in Aluminium 7075 metal matrix composites reinforced with submicron-TiB_2 particles. The results of their study revealed that the Ramakrishnan model and the Clyne model exhibited comparable results, both showing significant underestimations in predicting the rise in yield strength, particularly when the volume fraction of the reinforcing particles exceeded 0.5 vol%. On the contrary, the summation model and the Zhang-Chen model displayed a closer alignment with the experimental data, when the volume fraction of the reinforcing particles surpassed 0.7 vol%; however, still below the experimental observations. Sanaty-Zadeh [62] conducted a comparison of different yield strength prediction models, comparing their outcomes with data available in existing literature. The study revealed that the Clyne method demonstrated the closest alignment with the experimental data derived from the literature. In contrast, the summation method was observed to consistently overestimate the yield strength predictions, while the Zhang and Chen method underestimated the actual yield strength values. It is important to note that the Ramakrishna model and Zhang and Chen model do not take into account the complete spectrum of the strengthening mechanisms. Additionally, not all these strengthening mechanisms are interdependent, as assumed in the Clyne model. Moreover, when the reinforcing particles are sub-micron sized, as evident in this study, the reliability of the Clyne model may be doubtful [62]. Hence, the summation method is used in the present investigation as it offers a more suitable approach to approximate the increase in yield strength in the case of IN718/TiB_2.

Fig. 16 compares the tensile properties as observed in the present DED IN718 and IN718/TiB_2 with those as reported in the literature, including IN718 processed by different AM processes (DED, L-PBF and EBM) [3,4,9,11,12,14,39,75–80] and cast and wrought IN718 (AMS standard 5662 N) data [81]. This data comparison also includes MMCs such as IN718/SiC [35], IN718/Ti_2AlC [40], IN718/$CoAl_2O_4$ [36] and IN718/NbC [79]. All the data as summarised in Fig. 16 are from tensile tests where the loading direction was parallel to the build direction. The reason for the large variation in the yield strength and elongation is attributed to the deposition technique (DED, L-PBF) and the post-processing heat treatments. In the as-deposit condition, the yield strength of the AM IN718 varies from ~450 MPa to 800 MPa, while after the heat treatment, the yield strength is increased to ~1000 MPa–1250 MPa. The higher strength in heat-treated conditions is always at the cost of reduced ductility. The high yield strength observed in High Energy IN718/TiB_2-(V) from the current study is comparable to the wrought IN718 (AMS standard 5662 N) tested under heat-treated condition, despite being in an as-deposited condition.

The yield strength of L-PBF IN718/$CoAl_2O_4$ [36] is ~300 MPa lower than that observed in the present study. However, IN718/$CoAl_2O_4$ exhibits a very high ductility. The tensile strength of the L-PBF IN718/NbC in the as-built condition [79] is ~820 MPa, which increases to ~1400 MPa after the heat treatment; however, with a ductility reduction from ~20% to ~6%. The yield strength of ~950 MPa achieved in the IN718/TiB_2-(V) from the current study without any post-processing heat treatment is significantly higher than IN718 processed using various AM techniques and other IN718-based MMCs in the as-built condition. Therefore, the current investigation suggests an effective method to strengthen DED processed IN718 by adding 1.5 wt% TiB_2.

5. Conclusions

The present work explores the use of TiB_2 as an inoculant to fabricate IN718 via the blown-powder laser direct metal deposition (DED) process. The key findings in the as-deposit sample condition are summarised as follows:

1) The addition of TiB_2 to IN718 results in significant grain refinement and much reduced texture. Among the conditions investigated, a suitable TiB_2 powder size was found to be $d_{90} = 10$ μm with content of 1.5 wt%. A TiB_2 powder size of $d_{90} = 1$ μm or $d_{90} = 40$ μm results in agglomeration or detachment from the IN718 powder.
2) The powder flow rate during the deposition process affects the densification of the low-energy deposits ($E_l = 33.08$ J/mm). Interlayer defects are completely eliminated by reducing the powder flow rate from 12 g/min to 7 g/min.
3) The TiB_2 inoculant reduces the formation of large inter-dendritic Laves phase networks typical of DED IN718, by replacing it with a homogeneous distribution of Cr-, Mo-, Nb- and B-enriched needle-shaped precipitates. Under tensile loading, DED IN718 is subjected to micro-cracks initiated from the Laves phase, while for DED IN718/TiB_2 the micro-cracks appear at the interface between the needle-shaped precipitates and the matrix.
4) IN718/TiB_2 exhibits considerably higher hardness and improved tensile strength, at the cost of tensile ductility. Despite refined grains

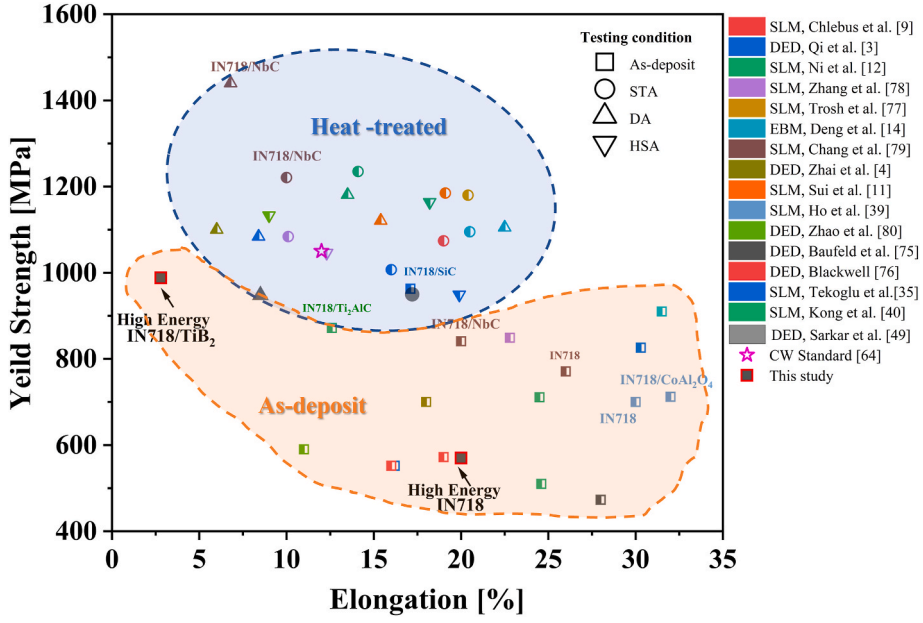

Fig. 16. Comparison of the tensile yield strength and ductility of the DED IN718 with and without the TiB_2 as the inoculant, obtained in the present work, with the literature data. Abbreviations of STA, DA and HSA stand for solution treated and aged, directly aged, and homogenised solution treated and aged, respectively.

with random texture in the IN718/TiB_2 deposit, anisotropy in tensile properties persists.

5) The contribution of individual strengthening mechanisms showed that, the dislocation structure formation, and Orowan type strengthening related to the needle-shaped precipitates in IN718/TiB_2 were the key contributors to the increased strength of IN718/TiB_2 along with minor contributions due to grain refinement and load transfer effect.

CRediT authorship contribution statement

Riddhi Sarkar: Conceptualization, Project administration, Data curation, Formal analysis, Investigation, Methodology, Visualization, Writing – original draft, Writing – review & editing. **Bo Chen:** Conceptualization, Supervision, Project administration, Visualization, Writing – original draft, Writing – review & editing. **Michael E. Fitzpatrick:** Conceptualization, Supervision, Project administration, Writing – review & editing. **Tim Hilditch:** Conceptualization, Project administration, Supervision, Writing – review & editing. **Daniel Fabijanic:** Conceptualization, Methodology, Project administration, Resources, Supervision, Writing – review & editing.

Declaration of competing interest

The authors declare that they have no known competing financial interests or personal relationships that could have appeared to influence the work reported in this paper.

Data availability

Data will be made available on request.

Acknowledgement

Riddhi Sarkar acknowledges the Deakin University Advanced Characterisation Facility for technical support. Bo Chen acknowledges the financial supports from the UK's Engineering and Physical Sciences Research Council, EPSRC Early Career Fellowship Scheme EP/R043973/1. MEF is grateful for the support of the Lloyd's Register Foundation, a charitable foundation helping to protect life and property by supporting engineering-related education, public engagement and the application of research.

References

[1] J.H. Yi, J.W. Kang, T.J. Wang, X. Wang, Y.Y. Hu, T. Feng, Y.L. Feng, P.Y. Wu, Effect of laser energy density on the microstructure, mechanical properties, and deformation of Inconel 718 samples fabricated by selective laser melting, J. Alloys Compd. 786 (2019) 481–488, https://doi.org/10.1016/j.jallcom.2019.01.377.

[2] E. Hosseini, V.A. Popovich, A review of mechanical properties of additively manufactured Inconel 718, Addit. Manuf. 30 (2019), 100877, https://doi.org/10.1016/j.addma.2019.100877.

[3] H. Qi, M. Azer, A. Ritter, Studies of standard heat treatment effects on microstructure and mechanical properties of laser net shape manufactured INCONEL 718, Metall. Mater. Trans. A Phys. Metall. Mater. Sci. 40 (2009) 2410–2422, https://doi.org/10.1007/s11661-009-9949-3.

[4] Y. Zhai, D.A. Lados, E.J. Brown, G.N. Vigilante, Understanding the microstructure and mechanical properties of Ti-6Al-4V and inconel 718 alloys manufactured by laser engineered net shaping, Addit. Manuf. 27 (2019) 334–344, https://doi.org/10.1016/j.addma.2019.02.017.

[5] G.P. Dinda, A.K. Dasgupta, J. Mazumder, Texture control during laser deposition of nickel-based superalloy, Scripta Mater. 67 (2012) 503–506, https://doi.org/10.1016/j.scriptamat.2012.06.014.

[6] M. Ni, C. Chen, X. Wang, P. Wang, R. Li, X. Zhang, K. Zhou, Anisotropic tensile behavior of in situ precipitation strengthened Inconel 718 fabricated by additive manufacturing, Mater. Sci. Eng. A. 701 (2017) 344–351, https://doi.org/10.1016/j.msea.2017.06.098.

[7] M.M. Kirka, F. Medina, R. Dehoff, A. Okello, Mechanical behavior of post-processed Inconel 718 manufactured through the electron beam melting process, Mater. Sci. Eng. A. 680 (2017) 338–346, https://doi.org/10.1016/j.msea.2016.10.069.

[8] D. Deng, R.L. Peng, H. Brodin, J. Moverare, Microstructure and mechanical properties of Inconel 718 produced by selective laser melting: sample orientation dependence and effects of post heat treatments, Mater. Sci. Eng. A. 713 (2018) 294–306, https://doi.org/10.1016/j.msea.2017.12.043.

[9] E. Chlebus, K. Gruber, B. Kuźnicka, J. Kurzac, T. Kurzynowski, Effect of heat treatment on the microstructure and mechanical properties of Inconel 718 processed by selective laser melting, Mater. Sci. Eng. A. 639 (2015) 647–655, https://doi.org/10.1016/j.msea.2015.05.035.

[10] G.H. Cao, T.Y. Sun, C.H. Wang, X. Li, M. Liu, Z.X. Zhang, P.F. Hu, A.M. Russell, R. Schneider, D. Gerthsen, Z.J. Zhou, C.P. Li, G.F. Chen, Investigations of γ′, γ″ and δ precipitates in heat-treated Inconel 718 alloy fabricated by selective laser melting, Mater. Char. 136 (2018) 398–406, https://doi.org/10.1016/j.matchar.2018.01.006.

[11] S. Sui, H. Tan, J. Chen, C. Zhong, Z. Li, W. Fan, A. Gasser, W. Huang, The influence of Laves phases on the room temperature tensile properties of Inconel 718 fabricated by powder feeding laser additive manufacturing, Acta Mater. 164 (2019) 413–427, https://doi.org/10.1016/j.actamat.2018.10.032.

[12] M. Ni, S. Liu, C. Chen, R. Li, X. Zhang, K. Zhou, Effect of heat treatment on the microstructural evolution of a precipitation-hardened superalloy produced by selective laser melting, Mater. Sci. Eng. A. 748 (2019) 275–285, https://doi.org/10.1016/j.msea.2019.01.109.

[13] W. Yang, P. Qu, L. Liu, Z. Jie, T. Huang, F. Wang, J. Zhang, Nucleation crystallography of Ni grains on CrFeNb inoculants investigated by edge-to-edge matching model in an IN718 superalloy, Adv. Eng. Mater. 20 (2018), 1700568, https://doi.org/10.1002/adem.201700568.

[14] D. Deng, J. Moverare, R.L. Peng, H. Söderberg, Microstructure and anisotropic mechanical properties of EBM manufactured Inconel 718 and effects of post heat treatments, Mater. Sci. Eng. A. 693 (2017) 151–163, https://doi.org/10.1016/j.msea.2017.03.085.

[15] K.V. Yang, Y. Shi, F. Palm, X. Wu, P. Rometsch, Columnar to equiaxed transition in Al-Mg(-Sc)-Zr alloys produced by selective laser melting, Scripta Mater. 145 (2018) 113–117, https://doi.org/10.1016/j.scriptamat.2017.10.021.

[16] W.J. Sames, F.A. List, S. Pannala, R.R. Dehoff, S.S. Babu, The metallurgy and processing science of metal additive manufacturing, Int. Mater. Rev. 61 (2016) 315–360, https://doi.org/10.1080/09506608.2015.1116649.

[17] M. Gäumann, C. Bezençon, P. Canalis, W. Kurz, Single-crystal laser deposition of superalloys: processing-microstructure maps, Acta Mater. 49 (2001) 1051–1062, https://doi.org/10.1016/S1359-6454(00)00367-0.

[18] L.L. Parimi, G. Ravi, D. Clark, M.M. Attallah, Microstructural and texture development in direct laser fabricated IN718, Mater. Char. 89 (2014) 102–111, https://doi.org/10.1016/j.matchar.2013.12.012.

[19] E.L. Stevens, J. Toman, A.C. To, M. Chmielus, Variation of hardness, microstructure, and Laves phase distribution in direct laser deposited alloy 718 cuboids, Mater. Des. 119 (2017) 188–198, https://doi.org/10.1016/j.matdes.2017.01.031.

[20] S. Sui, J. Chen, L. Ma, W. Fan, H. Tan, F. Liu, X. Lin, Microstructures and stress rupture properties of pulse laser repaired Inconel 718 superalloy after different heat treatments, J. Alloys Compd. 770 (2019) 125–135, https://doi.org/10.1016/j.jallcom.2018.08.063.

[21] S.S. Babu, N. Raghavan, J. Raplee, S.J. Foster, C. Frederick, M. Haines, R. Dinwiddie, M.K. Kirka, A. Plotkowski, Y. Lee, R.R. Dehoff, Additive manufacturing of nickel superalloys : opportunities for innovation and challenges related to qualification, Metall. Mater. Trans. A 49 (2018) 3764–3780, https://doi.org/10.1007/s11661-018-4702-4.

[22] L. Xi, P. Wang, K.G. Prashanth, H. Li, H.V. Prykhodko, S. Scudino, I. Kaban, Effect of TiB2 particles on microstructure and crystallographic texture of Al-12Si fabricated by selective laser melting, J. Alloys Compd. 786 (2019) 551–556, https://doi.org/10.1016/j.jallcom.2019.01.327.

[23] A. Hadadzadeh, B.S. Amirkhiz, J. Li, M. Mohammadi, Columnar to equiaxed transition during direct metal laser sintering of AlSi10Mg alloy: effect of building direction, Addit. Manuf. 23 (2018) 121–131, https://doi.org/10.1016/j.addma.2018.08.001.

[24] X.P. Li, G. Ji, Z. Chen, A. Addad, Y. Wu, H.W. Wang, J. Vleugels, J. Van Humbeeck, J.P. Kruth, Selective laser melting of nano-TiB2decorated AlSi10Mg alloy with high fracture strength and ductility, Acta Mater. 129 (2017) 183–193, https://doi.org/10.1016/j.actamat.2017.02.062.

[25] B. AlMangour, Y.K. Kim, D. Grzesiak, K.A. Lee, Novel TiB2-reinforced 316L stainless steel nanocomposites with excellent room- and high-temperature yield strength developed by additive manufacturing, Compos. Part B Eng. 156 (2019) 51–63, https://doi.org/10.1016/j.compositesb.2018.07.050.

[26] X. Li, H.J. Willy, S. Chang, W. Lu, T.S. Herng, J. Ding, Selective laser melting of stainless steel and alumina composite: experimental and simulation studies on processing parameters, microstructure and mechanical properties, Mater. Des. 145 (2018) 1–10, https://doi.org/10.1016/j.matdes.2018.02.050.

[27] B. Li, B. Qian, Y. Xu, Z. Liu, J. Zhang, F. Xuan, Additive manufacturing of ultrafine-grained austenitic stainless steel matrix composite via vanadium carbide reinforcement addition and selective laser melting: formation mechanism and strengthening effect, Mater. Sci. Eng. A. 745 (2019) 495–508, https://doi.org/10.1016/j.msea.2019.01.008.

[28] B. Almangour, D. Grzesiak, J.M. Yang, Rapid fabrication of bulk-form TiB2/316L stainless steel nanocomposites with novel reinforcement architecture and improved performance by selective laser melting, J. Alloys Compd. 680 (2016) 480–493, https://doi.org/10.1016/j.jallcom.2016.04.156.

[29] B. AlMangour, D. Grzesiak, J.M. Yang, Selective laser melting of TiB2/316L stainless steel composites: the roles of powder preparation and hot isostatic

pressing post-treatment, Powder Technol. 309 (2017) 37–48, https://doi.org/10.1016/j.powtec.2016.12.073.
[30] Q. Chao, S. Mateti, M. Annasamy, M. Imran, J. Joseph, Q. Cai, L.H. Li, P. Cizek, P. D. Hodgson, Y. Chen, D. Fabijanic, W. Xu, Nanoparticle-mediated ultra grain refinement and reinforcement in additively manufactured titanium alloys, Addit. Manuf. 46 (2021), 102173, https://doi.org/10.1016/j.addma.2021.102173.
[31] J.R. Kennedy, A.E. Davis, A.E. Caballero, S. Williams, E.J. Pickering, P. B. Prangnell, The potential for grain refinement of Wire-Arc Additive Manufactured (WAAM) Ti-6Al-4V by ZrN and TiN inoculation, Addit. Manuf. 40 (2021), 101928, https://doi.org/10.1016/j.addma.2021.101928.
[32] B. Li, B. Qian, Y. Xu, Z. Liu, F. Xuan, Fine-structured CoCrFeNiMn high-entropy alloy matrix composite with 12 wt% TiN particle reinforcements via selective laser melting assisted additive manufacturing, Mater. Lett. 252 (2019) 88–91, https://doi.org/10.1016/j.matlet.2019.05.108.
[33] Q. Chao, S. Mateti, M. Annasamy, M. Imran, J. Joseph, Q. Cai, L.H. Li, P. Cizek, P. D. Hodgson, Y. Chen, D. Fabijanic, W. Xu, Nanoparticle-mediated ultra grain refinement and reinforcement in additively manufactured titanium alloys, Addit. Manuf. 46 (2021), 102173, https://doi.org/10.1016/j.addma.2021.102173.
[34] T. Rong, D. Gu, Formation of novel graded interface and its function on mechanical properties of WC1-x reinforced Inconel 718 composites processed by selective laser melting, J. Alloys Compd. 680 (2016) 333–342, https://doi.org/10.1016/j.jallcom.2016.04.107.
[35] E. Tekoğlu, A.D. O'Brien, J. Liu, B. Wang, S. Kavak, Y. Zhang, S.Y. Kim, S. Wang, D. Ağaoğulları, W. Chen, A.J. Hart, J. Li, Strengthening additively manufactured Inconel 718 through in-situ formation of nanocarbides and silicides, Addit. Manuf. 67 (2023), 103478, https://doi.org/10.1016/j.addma.2023.103478.
[36] I.-T. Ho, Y.-T. Chen, A.-C. Yeh, C.-P. Chen, K.-K. Jen, Microstructure evolution induced by inoculants during the selective laser melting of IN718, Addit. Manuf. 21 (2018) 465–471, https://doi.org/10.1016/j.addma.2018.02.018.
[37] Q. Jia, D. Gu, Selective laser melting additive manufacturing of TiC/Inconel 718 bulk-form nanocomposites: densification, microstructure, and performance, J. Mater. Res. 29 (2014) 1960–1969, https://doi.org/10.1557/jmr.2014.130.
[38] D. Gu, G. Meng, C. Li, W. Meiners, R. Poprawe, Selective laser melting of TiC/Ti bulk nanocomposites: influence of nanoscale reinforcement, Scripta Mater. 67 (2012) 185–188, https://doi.org/10.1016/j.scriptamat.2012.04.013.
[39] I.T. Ho, T.H. Hsu, Y.J. Chang, C.W. Li, K.C. Chang, S. Tin, K. Kakehi, A.C. Yeh, Effects of CoAl2O4 inoculants on microstructure and mechanical properties of IN718 processed by selective laser melting, Addit. Manuf. 35 (2020), 101328, https://doi.org/10.1016/j.addma.2020.101328.
[40] Y. Kong, K. Peng, H. Huang, Additive manufacturing of high-strength Inconel 718 alloy through the addition of Ti2AlC MAX particles, J. Mater. Sci. Technol. 158 (2023) 180–193, https://doi.org/10.1016/j.jmst.2023.01.059.
[41] S. He, S. Park, D.S. Shim, C. Yao, W.J. Zhang, Study on microstructure and abrasive behaviors of inconel 718-WC composite coating fabricated by laser directed energy deposition, J. Mater. Res. Technol. 21 (2022) 2926–2946, https://doi.org/10.1016/j.jmrt.2022.10.088.
[42] F. Wang, J. Zhang, T. Huang, L. Liu, H. Fu, Preparation of inoculants used in superalloy and analysis of the atomic matching models, J. Mater. Sci. Technol. 29 (2013) 387–392, https://doi.org/10.1016/j.jmst.2013.02.007.
[43] Y. Xiong, J. Du, X. Wei, A. Yang, L. Liu, D. Zeng, Grain refinement of superalloy IN718C by the addition of inoculants, Metall. Mater. Trans. A Phys. Metall. Mater. Sci. 35 A (2004) 2111–2114, https://doi.org/10.1007/s11661-004-0159-8.
[44] Z. Zhang, Z. Liu, D. Wu, Prediction of melt pool temperature in directed energy deposition using machine learning, Addit. Manuf. 37 (2021), 101692, https://doi.org/10.1016/j.addma.2020.101692.
[45] M. Zhang, P. Kelly, M. Easton, J. Taylor, Crystallographic study of grain refinement in aluminum alloys using the edge-to-edge matching model, Acta Mater. 53 (2005) 1427–1438, https://doi.org/10.1016/j.actamat.2004.11.037.
[46] D. Gu, Y.-C. Hagedorn, W. Meiners, K. Wissenbach, R. Poprawe, Nanocrystalline TiC reinforced Ti matrix bulk-form nanocomposites by Selective Laser Melting (SLM): densification, growth mechanism and wear behavior, Compos. Sci. Technol. 71 (2011) 1612–1620, https://doi.org/10.1016/j.compscitech.2011.07.010.
[47] D. Gu, H. Zhang, D. Dai, M. Xia, C. Hong, R. Poprawe, Laser additive manufacturing of nano-TiC reinforced Ni-based nanocomposites with tailored microstructure and performance, Compos. Part B Eng. 163 (2019) 585–597, https://doi.org/10.1016/j.compositesb.2018.12.146.
[48] Y. Chen, Y. Guo, M. Xu, C. Ma, Q. Zhang, L. Wang, J. Yao, Z. Li, Study on the element segregation and Laves phase formation in the laser metal deposited IN718 superalloy by flat top laser and Gaussian distribution laser, Mater. Sci. Eng. A. 754 (2019) 339–347, https://doi.org/10.1016/j.msea.2019.03.096.
[49] R. Sarkar, B. Chen, M.E. Fitzpatrick, D. Fabijanic, T. Hilditch, Additive manufacturing-based repair of IN718 superalloy and high-cycle fatigue assessment of the joint, Addit. Manuf. 60 (2022), 103276, https://doi.org/10.1016/j.addma.2022.103276.
[50] Y. Chen, K. Zhang, J. Huang, S.R.E. Hosseini, Z. Li, Characterization of heat affected zone liquation cracking in laser additive manufacturing of Inconel 718, Mater. Des. 90 (2016) 586–594, https://doi.org/10.1016/j.matdes.2015.10.155.
[51] G.D. Janaki Ram, A. Venugopal Reddy, K. Prasad Rao, G.M. Reddy, J.K. Sarin Sundar, Microstructure and tensile properties of Inconel 718 pulsed Nd-YAG laser welds, J. Mater. Process. Technol. 167 (2005) 73–82, https://doi.org/10.1016/j.jmatprotec.2004.09.081.
[52] G.A. Knorovsky, M.J. Cieslak, T.J. Headley, A.D. Romig, W.F. Hammetter, Inconel 718: a solidification diagram, Metall. Trans. A 20 (1989) 2149–2158, https://doi.org/10.1007/BF02650300.
[53] C. Radhakrishna, K. Prasad Rao, The formation and control of Laves phase in superalloy 718 welds, J. Mater. Sci. 32 (1997) 1977–1984, https://doi.org/10.1023/A:1018541915113.
[54] H. Matysiak, M. Zagorska, A. Balkowiec, B. Adamczyk-Cieslak, K. Dobkowski, M. Koralnik, R. Cygan, J. Nawrocki, J. Cwajna, K.J. Kurzydlowski, The influence of the melt-pouring temperature and inoculant content on the macro and microstructure of the IN713C Ni-based superalloy, Jom 68 (2016) 185–197, https://doi.org/10.1007/s11837-015-1672-5.
[55] F. Gao, Z. Fan, Effect of nucleant particle agglomeration on grain size, Metall. Mater. Trans. A 53 (2022) 810–822, https://doi.org/10.1007/s11661-021-06549-2.
[56] S. Liu, X. Wang, C. Cui, L. Zhao, S. Liu, C. Chen, Fabrication, microstructure and refining mechanism of in situ CeB6/Al inoculant in aluminum, Mater. Des. 65 (2015) 432–437, https://doi.org/10.1016/j.matdes.2014.09.038.
[57] J. Yang, Q.Z. Wang, F.X. Yin, C.X. Cui, P.G. Ji, B. Li, Effects of grain refinement on the structure and properties of a CuAlMn shape memory alloy, Mater. Sci. Eng. A. 664 (2016) 215–220, https://doi.org/10.1016/j.msea.2016.04.009.
[58] J.A. Spittle, S. Sadli, Effect of alloy variables on grain refinement of binary aluminium alloys with Al–Ti–B, Mater. Sci. Technol. 11 (2012) 533–537, https://doi.org/10.1179/026708395790165273.
[59] B.P. Sahoo, D. Das, A.K. Chaubey, Strengthening mechanisms and modelling of mechanical properties of submicron-TiB2 particulate reinforced Al 7075 metal matrix composites, Mater. Sci. Eng. A. 825 (2021), 141873, https://doi.org/10.1016/j.msea.2021.141873.
[60] Y. Wang, Z. Liu, Y. Zhou, X. Yang, J. Tang, X. Liu, J. Li, G. Le, Microstructure and mechanical properties of TiN particles strengthened 316L steel prepared by laser melting deposition process, Mater. Sci. Eng. A. 814 (2021), 141220, https://doi.org/10.1016/j.msea.2021.141220.
[61] C.S. Goh, J. Wei, L.C. Lee, M. Gupta, Properties and deformation behaviour of Mg-Y2O3 nanocomposites, Acta Mater. 55 (2007) 5115–5121, https://doi.org/10.1016/j.actamat.2007.05.032.
[62] A. Sanaty-Zadeh, Comparison between current models for the strength of particulate-reinforced metal matrix nanocomposites with emphasis on consideration of Hall-Petch effect, Mater. Sci. Eng. A. 531 (2012) 112–118, https://doi.org/10.1016/j.msea.2011.10.043.
[63] Z. Zhang, D.L. Chen, Consideration of Orowan strengthening effect in particulate-reinforced metal matrix nanocomposites: a model for predicting their yield strength, Scripta Mater. 54 (2006) 1321–1326, https://doi.org/10.1016/j.scriptamat.2005.12.017.
[64] G.E. Dieter, Mechanical Metallurgy, McGraw-Hill, New York, 2011, https://doi.org/10.5962/bhl.title.35895.
[65] C. Li, Y. Tian, Y. Chen, P. Hodgson, X. Wu, Y. Zhu, A. Huang, Hierarchical layered and refined grain structure of Inconel 718 superalloy produced by rolling-assisted directed energy deposition, Addit. Manuf. Lett. 1 (2021), 100009, https://doi.org/10.1016/j.addlet.2021.100009.
[66] R. Zhao, J.Q. Han, B.B. Liu, M. Wan, Interaction of forming temperature and grain size effect in micro/meso-scale plastic deformation of nickel-base superalloy, Mater. Des. 94 (2016) 195–206, https://doi.org/10.1016/j.matdes.2016.01.022.
[67] R.W. Kozar, A. Suzuki, W.W. Milligan, J.J. Schirra, M.F. Savage, T.M. Pollock, Strengthening mechanisms in polycrystalline multimodal nickel-base superalloys, Metall. Mater. Trans. A Phys. Metall. Mater. Sci. 40 (2009) 1588–1603, https://doi.org/10.1007/s11661-009-9858-5.
[68] D.M. Bond, M.A. Zikry, Effects of electron beam manufacturing induced defects on fracture in Inconel 718, Addit. Manuf. 32 (2020), 101059, https://doi.org/10.1016/j.addma.2020.101059.
[69] R.K. Dutta, R.H. Petrov, R. Delhez, M.J.M. Hermans, I.M. Richardson, A.J. Böttger, The effect of tensile deformation by in situ ultrasonic treatment on the microstructure of low-carbon steel, Acta Mater. 61 (2013) 1592–1602, https://doi.org/10.1016/j.actamat.2012.11.036.
[70] J.H. Park, G.B. Bang, K.A. Lee, Y. Son, Y.H. Song, B.S. Lee, W.R. Kim, H.G. Kim, Effect of preheating temperature on microstructural and mechanical properties of inconel 718 fabricated by selective laser melting, Met. Mater. Int. (2022), https://doi.org/10.1007/s12540-022-01169-w.
[71] M.F. Ashby, Work hardening of dispersion-hardened crystals, Philos. Mag. A 14 (1966) 1157–1178, https://doi.org/10.1080/14786436608224282.
[72] Y. Li, D. Parfitt, P.E.J. Flewitt, X. Hou, J. Quinta de Fonseca, B. Chen, Microstructural considerations of enhanced tensile strength and mechanical constraint in a copper/stainless steel brazed joint, Mater. Sci. Eng. A. 796 (2020), https://doi.org/10.1016/j.msea.2020.139992.
[73] P. Kontis, H.A.M. Yusof, S. Pedrazzini, M. Danaie, K.L. Moore, P.A.J. Bagot, M. P. Moody, C.R.M. Grovenor, R.C. Reed, On the effect of boron on grain boundary character in a new polycrystalline superalloy, Acta Mater. 103 (2016) 688–699, https://doi.org/10.1016/j.actamat.2015.10.006.
[74] N. Ramakrishnan, An analytical study on strengthening of particulate reinforced metal matrix composites, Acta Mater. 44 (1996) 69–77, https://doi.org/10.1016/1359-6454(95)00150-9.
[75] B. Baufeld, Mechanical properties of INCONEL 718 parts manufactured by shaped metal deposition (SMD), J. Mater. Eng. Perform. 21 (2012) 1416–1421, https://doi.org/10.1007/s11665-011-0009-y.
[76] P.L. Blackwell, The mechanical and microstructural characteristics of laser-deposited IN718, J. Mater. Process. Technol. 170 (2005) 240–246, https://doi.org/10.1016/j.jmatprotec.2005.05.005.
[77] T. Trosch, J. Strößner, R. Völkl, U. Glatzel, Microstructure and mechanical properties of selective laser melted Inconel 718 compared to forging and casting, Mater. Lett. 164 (2016) 428–431, https://doi.org/10.1016/j.matlet.2015.10.136.

[78] D. Zhang, W. Niu, X. Cao, Z. Liu, Effect of standard heat treatment on the microstructure and mechanical properties of selective laser melting manufactured Inconel 718 superalloy, Mater. Sci. Eng. A. 644 (2015) 32–40, https://doi.org/10.1016/j.msea.2015.06.021.

[79] K.C. Chang, M.Y. Lee, T.H. Hsu, Y.J. Chang, K.C. Lo, H.S. Kim, K.K. Jen, A.C. Yeh, An effective strengthening strategy of nano carbide precipitation and cellular microstructure refinement in a superalloy fabricated by selective laser melting process, Metals (Basel) 11 (2021), https://doi.org/10.3390/met11111691.

[80] X. Zhao, J. Chen, X. Lin, W. Huang, Study on microstructure and mechanical properties of laser rapid forming Inconel 718, Mater. Sci. Eng. A. 478 (2008) 119–124, https://doi.org/10.1016/j.msea.2007.05.079.

[81] SAE International, AMS5662N: Nickel Alloy, Corrosion and Heat-Resistant, Bars, Forgings, and Rings 52.5Ni - 19Cr - 3.0Mo - 5.1Cb (Nb) - 0.90Ti - 0.50AI - 18Fe Consumable Electrode or Vacuum Induction Melted 1775 F (968 C) Solution Heat Treated, Precipitation-Hardenable, 2016.